



Global trends of ocean CO₂ sink and ocean acidification: an observation-based reconstruction of surface ocean inorganic carbon variables

Yosuke Iida^{1,2} · Yusuke Takatani³ · Atsushi Kojima¹ · Masao Ishii^{1,2}

Received: 26 December 2019 / Revised: 8 October 2020 / Accepted: 12 October 2020 / Published online: 18 November 2020
© The Oceanographic Society of Japan and Springer Nature Singapore Pte Ltd. 2020

Abstract

Ocean acidification is likely to impact marine ecosystems and human societies adversely and is a carbon cycle issue of great concern. Projecting the degree of ocean acidification and the carbon-climate feedback will require understanding the current status, variability, and trends of ocean inorganic carbon system variables and the ocean carbon sink. With this goal in mind, we reconstructed total alkalinity (TA), dissolved inorganic carbon (DIC), CO₂ partial pressure ($p\text{CO}_2\text{sea}$), sea–air CO₂ flux, pH, and aragonite saturation state (Ω_{arg}) for the global ocean based on measurements of $p\text{CO}_2\text{sea}$ and TA. We used a multiple linear regression approach to derive relationships to explain TA and DIC and obtained monthly $1^\circ \times 1^\circ$ gridded values of TA and DIC for the period 1993–2018. These data were converted to $p\text{CO}_2\text{sea}$, pH, and Ω_{arg} , and monthly sea-air CO₂ fluxes were obtained in combination with atmospheric CO₂. Mean annual sea–air CO₂ flux and its rate of change were estimated to be $-2.0 \pm 0.5 \text{ PgC year}^{-1}$ and $-0.3 \text{ (PgC year}^{-1}) \text{ decade}^{-1}$, respectively. Our analysis revealed that oceanic CO₂ uptake decreased during the 1990s and has been increasing since 2000. Our estimate of the globally averaged rate of pH change, $-0.0181 \pm 0.0001 \text{ decade}^{-1}$, was consistent with that expected from the trend of atmospheric CO₂ growth. However, rates of decline of pH were relatively slow in the Southern Ocean ($-0.0165 \pm 0.0001 \text{ decade}^{-1}$) and in the western equatorial Pacific ($-0.0148 \pm 0.0002 \text{ decade}^{-1}$). Our estimate of the globally averaged rate of pH change can be used to verify Indicator 14.3.1 of Sustainable Development Goals.

Keywords Ocean acidification · Ocean carbon sink · SOCAT · SOCOM · SDGs

1 Introduction

The ocean has stored approximately 30% of the total CO₂ released by human industrial activities during the industrial era (Khatiwala et al. 2013) and has therefore played a significant role in slowing the growth of CO₂ concentrations in the atmosphere and mitigating global warming. However, this uptake of CO₂ has endangered the health of the

ocean through what is referred to as ocean acidification. The absorption of anthropogenic CO₂ into seawater increases its acidity (reduces its pH), reduces the saturation levels of calcium carbonate minerals, and is thus very likely to have a variety of adverse impacts on marine ecosystems and human societies (Gattuso et al. 2015). In 2015, the United Nations adopted The 2030 Agenda for Sustainable Development. In the agenda, ocean acidification is target 3 of goal 14, and this target is accompanied by an indicator of global average oceanic pH for SDG 14.3 (United Nations 2015; IOC/UNESCO 2018). A key challenge is to better understand contemporary trends of ocean acidification globally to project future trends in a more informed way.

The change of oceanic CO₂ uptake and its impact on the global carbon budget in the future have been other great concerns because they are closely related to global warming projections. Gruber et al. (2019a) have shown that the mean rate of global oceanic CO₂ storage for the period 1994–2007 is consistent with the expected increase in ocean uptake,

✉ Yosuke Iida
iida-ysk@met.kishou.go.jp

¹ Global Environment and Marine Department, Japan Meteorological Agency, 1-3-4 Otemachi Chiyoda-ku, Tokyo 100-8122, Japan

² Climate and Geochemistry Research Department, Meteorological Research Institute, 1-1 Nagamine, Tsukuba, Ibaraki 305-0052, Japan

³ Forecast Department, Japan Meteorological Agency, 1-3-4 Otemachi Chiyoda-ku, Tokyo 100-8122, Japan

which is proportional to the increase of the atmospheric CO_2 concentration. However, earth system models run under the RCP 8.5 scenario project that oceanic CO_2 uptake will not grow, and therefore the ratio of oceanic CO_2 uptake to anthropogenic CO_2 emissions will decrease significantly after roughly the year 2070 (Wang et al. 2016; Schlunegger et al. 2019).

Although oceanic carbon measurements have been conducted around the world for many years, synthesized datasets of sufficient quality to facilitate evaluation of the perturbations caused by anthropogenic CO_2 emissions have become available only since the early 2000s. The Global Ocean Data Analysis Project version 2 (GLODAP v2), which has been a successor to the GLODAP (Key et al. 2004), CARINA (Key et al. 2010), and PACIFICA (Suzuki et al. 2013) projects, has completed the synthesis of high-quality carbon measurements for the interior of the global ocean during past decades (Olsen et al. 2016), and that dataset has been updated as version 2019 (GLODAP v2.2019: Olsen et al. 2019). Data synthesis of surface CO_2 measurements, i.e., Surface Ocean CO_2 Atlas (SOCAT), which contains data from 1950s through recent past, has also been run from 2000s by community efforts (Bakker et al. 2016). These synthesized datasets have been used for numerous studies of the dynamics of global and regional carbon cycles.

Several methods have been developed for the interpolation and extrapolation of surface ocean CO_2 partial pressure ($p\text{CO}_{2\text{sea}}$) measurements to investigate the variability of the oceanic CO_2 sink. An intercomparison exercise, the Surface Ocean $p\text{CO}_2$ Mapping Intercomparison (SOCOM), has been conducted during 2010s (Rödenbeck et al. 2015). One of the methods was developed by Iida et al. (2015), who derived empirical equations for mapping global $p\text{CO}_{2\text{sea}}$ fields using a multiple linear regression (MLR) method with sea surface temperature (SST), sea surface salinity (SSS), and

chlorophyll-*a* (Chl) as independent variables and explicitly taking into account secular trends caused by the accumulation of anthropogenic CO_2 in the ocean. However, $p\text{CO}_{2\text{sea}}$ changes as a thermodynamic function of temperature, salinity, total alkalinity (TA), and the concentration of dissolved inorganic carbon (DIC). Statistical relationships often conflict with thermodynamic relationships in areas such as subpolar and the equatorial divergence zones, where winter vertical mixing or upwelling lowers temperature but raises $p\text{CO}_{2\text{sea}}$. More importantly, the CO_2 buffering capacity of seawater is decreasing with the accumulation of anthropogenic CO_2 in the ocean, and hence the thermodynamic sensitivities of $p\text{CO}_{2\text{sea}}$ to temperature change and to CO_2 uptake/release are increasing. Consequently, the amplitude of the seasonal and interannual variability of $p\text{CO}_{2\text{sea}}$ is increasing (Rodgers et al. 2008; Landschützer et al. 2018). These changes in thermodynamic equilibria involving $p\text{CO}_{2\text{sea}}$ make it difficult in principle for a single set of empirical equations for $p\text{CO}_{2\text{sea}}$ to be applied over a timeframe of decades during which there are significant increases of $p\text{CO}_{2\text{sea}}$. Furthermore, increasing concern about the progress of ocean acidification in recent years has added to the importance of accurately mapping the spatiotemporal variability of $p\text{CO}_{2\text{sea}}$, sea-air CO_2 fluxes, pH, and the saturation state of aragonite (Ω_{arg}) (e.g., Takahashi et al. 2014).

In this work, we attempted to empirically reconstruct the fields of TA (or salinity-normalized TA: $n\text{TA}$, where $n\text{TA} = \text{TA}/\text{SSS} \times 35$) and DIC (or salinity-normalized DIC: $n\text{DIC}$, where $n\text{DIC} = \text{DIC}/\text{SSS} \times 35$) based on the measurements, and then to reconstruct the fields of $p\text{CO}_{2\text{sea}}$, pH, and Ω_{arg} from the fields of $n\text{TA}$, $n\text{DIC}$, SST, and SSS (Fig. 1; Table 1). Sea-air CO_2 flux fields were then reconstructed. Fields of TA were reconstructed from measurement data using MLR methods (e.g., Millero et al. 1998; Lee et al. 2006; Fry et al. 2016). Takatani et al. (2014) have

Fig. 1 Schematic description of the data flow for deriving surface ocean inorganic carbon variables and sea-air CO_2 flux products. Light blue, orange, and green arrows indicate the flow of the estimation of (1) alkalinity, (2) DIC, and (3) ocean acidification parameters and CO_2 fluxes. Abbreviations are listed in the caption for Table 1 (color figure online)

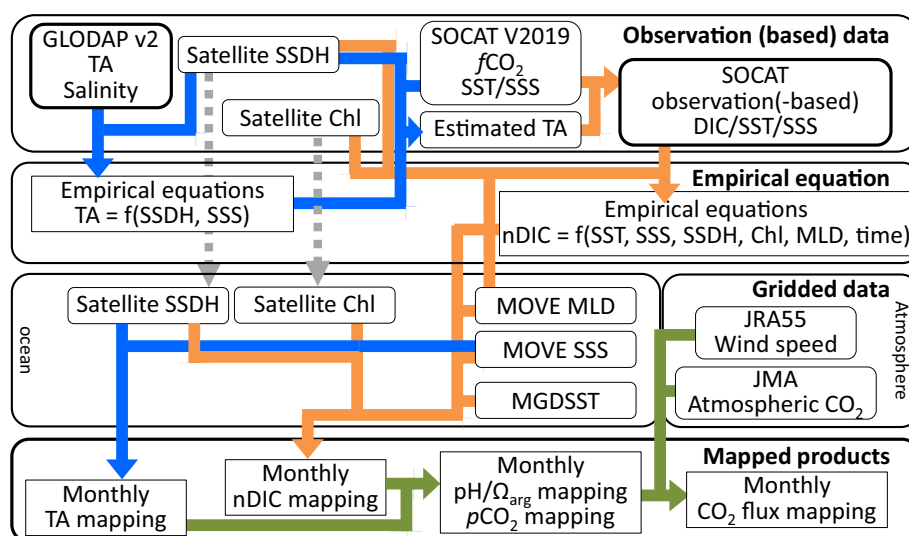


Table 1 List of data used for this study

Components	Dataset names	Website	References
In situ $f\text{CO}_2$ /SST/SSS	SOCAT V2019 ^a	https://www.socat.info/	Bakker et al. (2016)
In situ TA/SSS	GLODAPv2.2019 ^b	https://www.nodc.noaa.gov/ocads/oceans/GLODAPv2_2019/	Olsen et al. (2019)
Nutrients climatology	WOA18 ^c	https://www.nodc.noaa.gov/OC5/woa18/	Garcia et al. (2018)
Gridded SST	MGDSST ^d	https://ds.data.jma.go.jp/gmd/goos/data/datab ase.html	Sakurai et al. (2007)
Gridded SSS and MLD	MOVE/MRI.COM-G2 ^e	https://ds.data.jma.go.jp/gmd/goos/data/datab ase.html	Toyoda et al. (2013)
Gridded SSDH	JMA SSHA AVISO MDT	https://ds.data.jma.go.jp/gmd/goos/data/datab ase.html https://www.aviso.altimetry.fr	Kuragano and Kamachi (2000) Rio et al. (2014)
Chlorophyll- <i>a</i>	SeaWiFS MODIS/Aqua VIIRS, MERIS	https://globcolour.info	Maritorena et al. (2010)
Sea level pressure 10 m wind speed	JRA55 ^f	https://jra.kishou.go.jp/JRA-55/index_en.html	Kobayashi et al. (2015)
Atmospheric CO ₂	JMA global CO ₂	https://ds.data.jma.go.jp/ghg/kanshi/co2data/co2_mapdata_e.html	Nakamura et al. (2015)

^aSurface Ocean CO₂ Atlas version 2019

^bGlobal Ocean Data Analysis Project version 2 update 2019

^cWorld Ocean Atlas 2018

^dMerged satellite and in situ data Global Daily Sea Surface Temperatures

^eMultivariate Ocean Variational Estimation system/Meteorological Research Institute Community Ocean Model

^fthe Japanese 55-year Reanalysis

reconstructed TA fields in the surface layer of the Pacific by using sea surface dynamic height (SSDH) and SSS as explanatory variables to ensure compatibility with ocean circulation and to avoid the use of longitudinal and latitudinal borders that could have created artificial discontinuities in the TA distribution.

Here, we derive statistical relationships to estimate surface TA by an extension of the approach of Takatani et al. (2014) to the global open ocean. Subsequently, we calculate nDIC from TA values derived from the equations and CO₂ fugacity ($f\text{CO}_2$) data stored in SOCAT. We then derive equations to estimate nDIC using MLR methods and oceanographic variables such as SST, SSS, SSDH, Chl, and mixed layer depth (MLD) as explanatory variables. The sea-air CO₂ flux is then estimated from the $p\text{CO}_2$ sea calculated from DIC and TA in combination with the atmospheric $p\text{CO}_2$ and gas exchange coefficients across the sea-air interface that were calculated as a function of wind speed. Finally, we calculate the values of inorganic carbon variables including pH and Ω_{arg} . The global and basin scale oceanic CO₂ sink is obtained by integrating the flux over the relevant area, and the trends in pH and Ω_{arg} are derived by averaging the anomaly from the climatologies of mapped data. The same approach has been applied for the quasi-time series data from 137° E in the western North Pacific to assess the trend of accelerating ocean acidification (Ono et al. 2019).

These estimates not only help understand the change in the ocean carbon cycle, but also make it possible to evaluate SDG indicator 14.3.1 (Wanninkhof et al. 2019).

2 Data production methods

2.1 Derivation of equations to estimate TA

Takatani et al. (2014) have developed equations to estimate surface TA in the Pacific Ocean and the Pacific sector of the Southern Ocean by using a synthesized and quality-controlled dataset of interior-ocean carbonate system measurements made as a part of the PACIFICA project (Suzuki et al. 2013) and satellite SSDH data (Kuragano and Kamachi 2000). They used SSDHs to define ocean regimes and derived independent equations for each regime. SSDHs are useful for expressing the variability of wind-driven circulation and eddies (e.g., Kida et al. 2015) that are associated with variations in the distribution of surface nTA. We also used SSDH as an explanatory variable in our MLR, in accordance with the method of Takatani et al. (2014). We used TA data that had been adjusted for analytical offsets and stored in the GLODAPv2.2019 database (Olsen et al. 2019).

We extracted data from the surface layer (<25 m) by using the datum from the shallowest depth at each station and not using data from below the mixed layer, i.e., the depth at which the increase in σ_θ from the surface (10 m) reached 0.03 kg m^{-3} . As found by Takatani et al. (2014) in the Pacific Ocean and Southern Ocean, nTA was negatively correlated with SSDH, except in areas of the subtropics where nTA was low and nearly constant at $\sim 2300 \text{ } \mu\text{mol}\cdot\text{kg}^{-1}$ (Fig. 2). Some nTA data from the subpolar region were scattered within a narrow range of SSDHs but where there were variations of SSS. In this study, we used definitions of oceanic zones in the Pacific and Southern Ocean that were similar to but slightly modified from those in Takatani et al. (2014). In a way similar to our use of SSDHs to define zones in the Pacific Ocean, we defined four and two zones in the Atlantic and Indian Ocean, respectively (Fig. 3; Table 4).

Consequently, nTA was fit to Eq. 1, which uses SSDH and SSS as explanatory variables.

$$\text{nTA} = a + b \times \text{SSDH} + c \times \text{SSS}. \quad (1)$$

Constant values of nTA (i.e., the parameters b and c in Eq. 1 set to zero) were applied to areas with small nTA variability, such as the subtropics of the Atlantic, the Indian and Pacific Oceans, and the subarctic Pacific. Some zones needed both variables, and others needed either SSDH or SSS (see Appendix 1 for details).

2.2 Derivation of equations to estimate DIC

The GLODAPv2.2019 database also contains high-quality DIC data and can be used to derive statistical relationships between nDIC and other variables. However, the number of discrete DIC measurements is not large enough to perform regressions with small standard errors because nDIC is more variable in space and time than nTA (e.g., Sarmiento and Gruber 2006), and many more data are required to derive usable relationships. We therefore used the $f\text{CO}_2$ data with flags A to D stored in the SOCAT V2019 database, which is a quality-controlled surface $f\text{CO}_2$ dataset and contains 25.7 million data of measurements in global oceans over

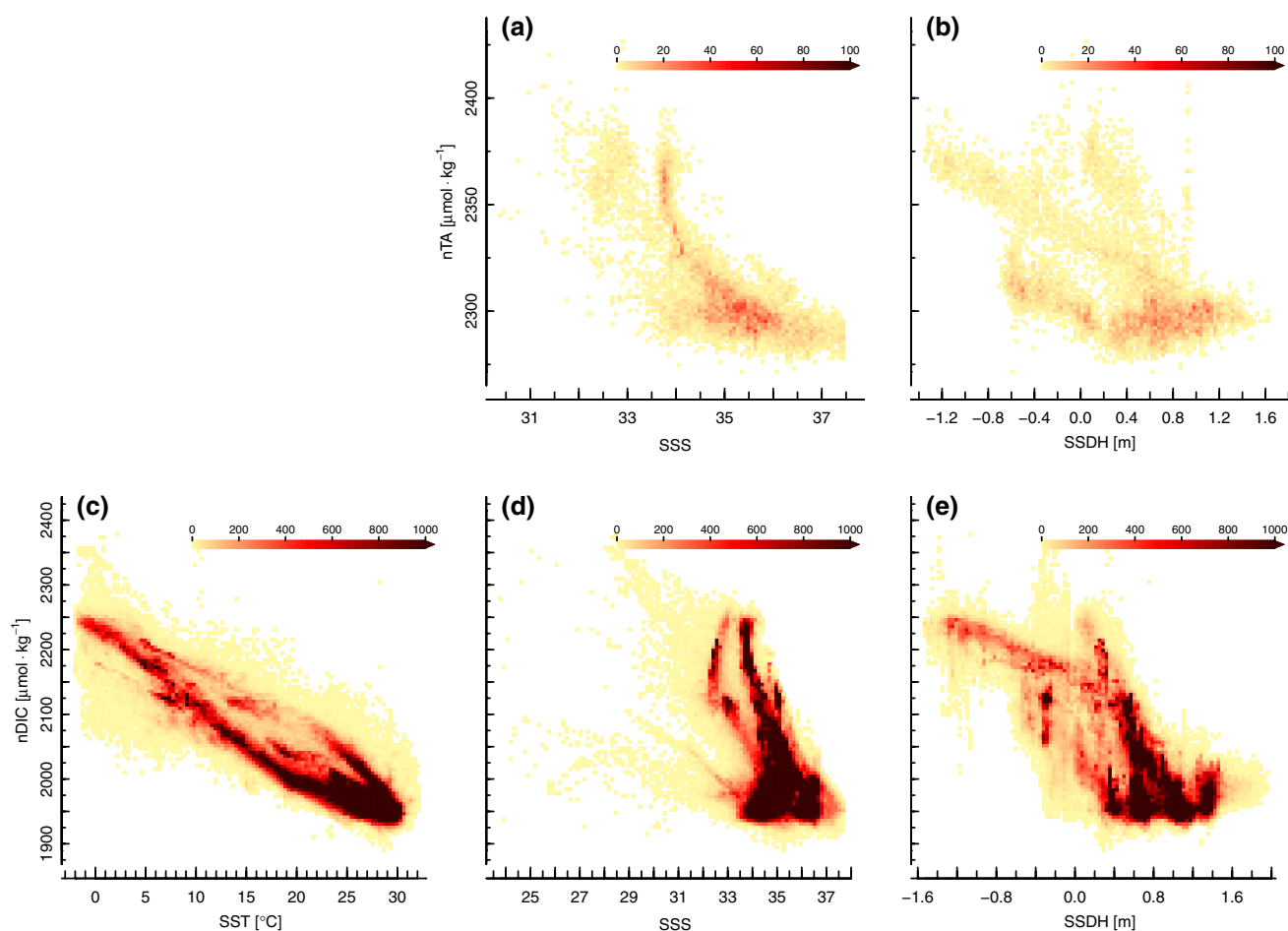


Fig. 2 Relationships between nTA or nDIC and other variables; **a**: nTA and SSS, **b**: nTA and SSDH, **c**: nDIC and SST, **d**: nDIC and SSS, and **e**: nDIC and SSDH. Coloring indicates number of data points in a grid

the period from 1957 to 2019 (Bakker et al. 2016). We converted the $f\text{CO}_2$ values into DIC by coupling them with the TAs calculated from the equations mentioned in Sect. 2.1 with the SSTs and SSSs in the SOCAT database and climatological phosphate and silicate concentrations taken from the World Ocean Atlas 2018 (WOA18; Garcia et al. 2018) based on seawater CO₂ chemistry. For the equilibrium calculation, we used the R seacarb package (seacarb 3.2.12; Gattuso et al. 2019) with default dissociation constants.

The fact that the correlations between nDIC and SST were generally negative (Fig. 2c) indicates that SST is a key explanatory variable for the empirical estimation of nDIC. The negative correlation in part reflects upwelling of cold, nDIC-rich subsurface seawaters to the surface in regions with eastern boundary currents, in the equatorial divergence zone, and in the Arabian Sea (e.g., Alin et al. 2012; Feely et al. 2006; Ishii et al. 2004; Sarma 2003). Convective deep mixing in winter also brings subsurface seawater with lower temperatures and higher DIC to the surface (e.g., Ishii et al. 2011). The use of other physical parameters, including SSDH, SSS, and MLD as explanatory variables, can yield zone-dependent equations that fit data better. For instance, MLD is also a useful explanatory variable in regions such as the northern subtropics and subarctic, especially in the northern North Atlantic (e.g., Olsen et al. 2008). In offshore regions that are subjected to the influence of river discharge, the mixture of river water and seawater has a nDIC/salinity ratio that is higher than expected from the evaporation-precipitation line because river water has a lower salinity than seawater but a substantial DIC content (e.g., Bates et al. 2006; Ibánhez et al. 2015; Kosugi et al. 2016; Chou et al. 2017). In subarctic regions and in the Southern Ocean, where net biological consumption of DIC is prominent especially in summer (e.g., Takahashi et al. 2002), a DIC that is lower than expected from the SST-nDIC relationship is often observed (e.g., Fay and McKinley 2017), and incorporation of Chl as another explanatory variable leads to better fits. What is also critical in empirically mapping nDIC is that it has been increasing with time because of the uptake of anthropogenic CO₂. The rate of nDIC increase due to anthropogenic CO₂ uptake is potentially different among zones because of differences in CO₂ buffering capacity and ocean circulation. We therefore defined a total of 57 smaller zones (subzones) for nDIC by sub-dividing the 14 nTA zones to take into account the characteristics of nDIC variations and by using mainly SSDH distributions as borders (Fig. 3). We also used SST and SSS as indicators to define the subzones of nutrient depletion (e.g., Lee et al. 2002), the equatorial cold tongue (e.g., Inoue et al. 1996; Ishii et al. 2009), and large river plumes (e.g., Körtzinger 2003) that vary with time. Apparent relationships between nDIC and other ocean variables are unique to each subzone. We then developed MLR equations to estimate nDIC from those variables.

$$\text{nDIC} = f(\text{time, SST, SSS, SSDH, Chl, MLD}). \quad (2)$$

We calculated MLDs from the ocean data assimilation system (MOVE/MRI.COM-G; Toyoda et al. 2013) by using a density-based MLD definition (de Boyer Montégut et al. 2004): the depth at which the density exceeds surface $\sigma_\theta + 0.03 \text{ kg m}^{-3}$. Chl data were obtained from satellite observations (Table 1; Fig. 1). We selected appropriate variables used in each MLR based on possible oceanographic processes that would occur in each subzone. We derived nDIC distributions by using time-varying subzones based on oceanic parameters (not based on meridional and/or parallel borders) (Fig. 3). Further details about the derivation of the equations are described in Appendix 2.

2.3 Mapping inorganic carbon variables

The monthly fields of nTA and nDIC ($1^\circ \times 1^\circ$ in longitude and latitude) were derived by applying global gridded datasets of SST, SSS, SSDH, Chl, and MLD to the empirical relationships for nTA and nDIC (Table 1; Fig. 1). The monthly fields of pH in total scale, $p\text{CO}_{2\text{sea}}$, and Ω_{arg} were then calculated from the fields of nTA, nDIC, SST, and SSS based on seawater CO₂ chemistry. We also calculated the sea-air CO₂ flux (F) by using the bulk formula Eq. 3:

$$F = k \times L \times (p\text{CO}_{2\text{sea}} - p\text{CO}_{2\text{air}}), \quad (3)$$

where k denotes the gas transfer velocity expressed as a function of the wind speed 10 m above sea level (U_{10}), L denotes the solubility of CO₂ (Weiss 1974), and $p\text{CO}_{2\text{air}}$ denotes the $p\text{CO}_2$ of air above the sea surface derived from atmospheric inversion analysis (Nakamura et al. 2015). Whereas several equations have been proposed to parameterize k as a function of U_{10} , we used Eq. 4, which was proposed by Wanninkhof (2014), in which k is proportional to U_{10}^2 . This equation has been widely used to estimate CO₂ fluxes from regional to global scales (e.g., Rödenbeck et al. 2015) and has been compared with direct flux measurements (e.g., Prytherch et al. 2017).

$$k = a \times U_{10}^2 \times \left(\frac{Sc}{660} \right)^{-0.5}. \quad (4)$$

In Eq. 4, a denotes a scaling factor. A correction to fit to the wind fields of the Japanese 55-year Reanalysis (JRA55; Kobayashi et al. 2015) was made according to Iida et al. (2015), and a value of 0.259 for a was derived. $\langle U_{10}^2 \rangle$ denotes the second moment of the wind speed averaged monthly within $1^\circ \times 1^\circ$ quadrats, and Sc denotes the Schmidt number (i.e., the inverse of the ratio of the CO₂ molecular diffusion coefficient to seawater kinematic viscosity) calculated from SST based on the equation proposed by Wanninkhof (2014).

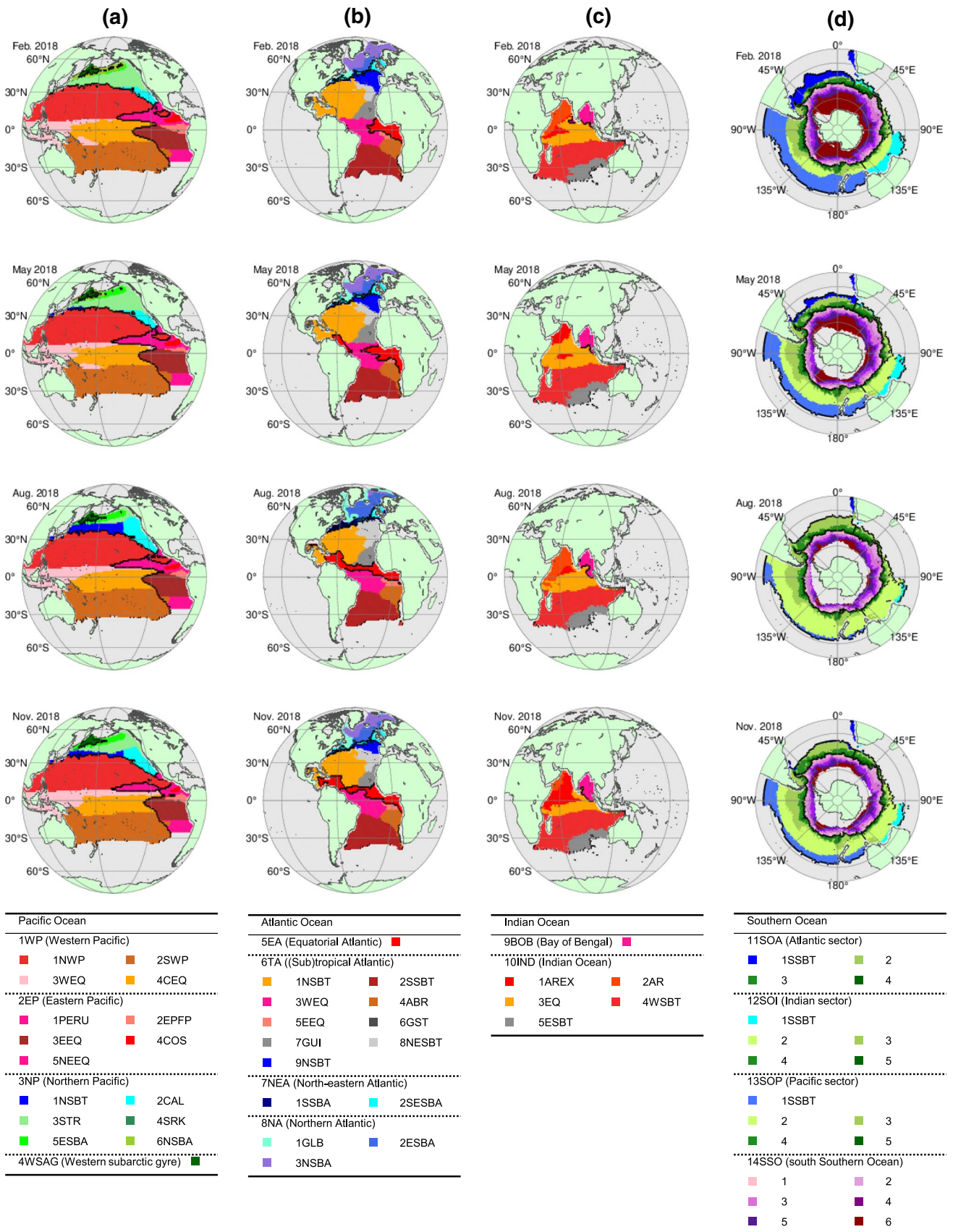


Fig. 3 Illustration of monthly maps of zones and subzones for nTA and nDIC estimation for the **a** Pacific, **b** Atlantic, **c** Indian and **d** Southern Oceans during the representative months of February, May, August, and November of 2018. Black lines show borders of zones for nTA estimation and colouring indicates subzones for nDIC estimation. Note that some colors for nDIC subzones are used in more than one basin. Legends of colors are shown at the bottom. Abbreviations of zones and subzones in the legends are defined in the text (color figure online)

2.4 Evaluation of decadal trends of ocean acidification

After $1^\circ \times 1^\circ$ gridded monthly pH and Ω_{arg} fields were obtained, we calculated their rates of change over past decades. First, we detrended the seasonal and regional variabilities of pH and Ω_{arg} by calculating the anomalies of their monthly values for each $1^\circ \times 1^\circ$ grid, and then these anomalies were integrated over the basins and the whole ocean to calculate basin and global scale trends of ocean acidification. We also calculated hypothetical trends of pH on the assumption that $p\text{CO}_2\text{sea}$ was in instantaneous equilibrium with the growth of atmospheric CO₂ using the same fields of nTA, SST, and SSS.

3 Results

3.1 Validation of the method

3.1.1 Uncertainty in estimating inorganic carbon variables

We used six explanatory variables in the MLRs to estimate nDIC. The use of many variables possibly causes overfitting and/or multicollinearity. However, we confirmed that the effect of these potential problems was minimal by checking the variance inflation factors in the regressions and the property–property plots between the mapped DICs and gridded variables that were used for the reconstruction. To assess the uncertainty associated with the reconstruction of inorganic carbon variables, robust statistics of bias and median absolute deviation (σ) averaged over time and space for a parameter A were evaluated using Eqs. 5 and 6.

$$\text{bias} = \text{median}(A_{\text{est}} - A_{\text{obs}}), \quad (5)$$

$$\sigma = 1.4826 \cdot \text{median}|A_{\text{est}} - A_{\text{obs}}|, \quad (6)$$

where the factor 1.4826 was used to ensure comparability with the standard deviation of the normal distribution (e.g., Leys et al. 2013).

Two potential sources of uncertainty were (a) uncertainty associated with regression analysis, and (b) discrepancy between gridded and measured SSTs and SSSs. The former

can be quantified by comparing the measured nDICs with the nDICs estimated from the measured SSTs, SSSs, and other variables. That metric corresponds to the standard error of the MLR. The latter can be quantified by comparing the measured nDICs with the nDICs estimated using gridded SSTs and SSSs instead of the observed SSTs and SSSs. In addition, we considered three ways to validate the estimation: (1) using regressions to check the reproducibility of input data. This check was carried out by comparing measured nDIC values with nDICs calculated from empirical equations. The metric therefore had the same meaning as the standard error of the MLR; (2) comparing 10% of subsampled nDIC data for validation with nDICs calculated from the equations derived using the other 90% of the data for learning; and (3) comparing the results with independent data from another source, such as GLODAPv2.2019 DIC measurements.

The globally calculated σ (reproducibility of MLR) for TA estimation was $5.8 \mu\text{mol kg}^{-1}$. This σ was comparable to the σ 's estimated with other interpolation methods, such as the σ 's of 8.1 and $7.8 \mu\text{mol kg}^{-1}$ reported by Lee et al. (2006) and Takatani et al. (2014), respectively. The TAs estimated more recently (e.g., Fry et al. 2016; Carter et al. 2018; Broullón et al. 2019) were also associated with comparable uncertainties. The biases of most grids were small, i.e., within $\pm 10 \mu\text{mol kg}^{-1}$, but the σ 's of some grids in off California, subarctic regions, and the Bay of Bengal were larger than $20 \mu\text{mol kg}^{-1}$ (Fig. 4a). In these regions, there were large variations in the values of SSDH and/or SSS that reflected rapid changes in ocean circulation. These variabilities led to discrepancies between the values of SSDH and/or SSS at the time of the TA observations and the monthly mean values.

The biases for nDIC estimation were similar to those for nTA: they were generally small, but the σ 's exceeded $20 \mu\text{mol kg}^{-1}$ in high latitudes and equatorial divergence zones (Fig. 4b). These high σ values reflected variability of CO₂ chemistry on a spatiotemporal scale smaller than 1° in space and shorter than one month in time that may be associated with photosynthesis and upwelling in these regions. The globally averaged σ 's based on the MLR were $6.1 \mu\text{mol kg}^{-1}$, $10.9 \mu\text{atm}$, 0.011 , and 0.06 for nDIC, $p\text{CO}_2\text{sea}$, pH, and Ω_{arg} , respectively (Table 2). These values were confirmed by comparing with the σ 's from the subsampling method ($5.9 \mu\text{mol kg}^{-1}$, $10.8 \mu\text{atm}$, 0.011 , and 0.06 , respectively). When integrated globally, SST and SSS themselves had small biases of -0.05°C and $+0.01$, respectively, but regionally uneven biases of SST and SSS caused relatively large dispersions of nDIC. If the discrepancies between the measured and gridded SSTs and SSSs were taken into account, the errors in nDIC, $p\text{CO}_2\text{sea}$, pH, and Ω_{arg} were $8.2 \mu\text{mol kg}^{-1}$, $12.1 \mu\text{atm}$, 0.012 , and 0.08 , respectively. The σ for $p\text{CO}_2\text{sea}$ calculated by the MLR was comparable with those estimated

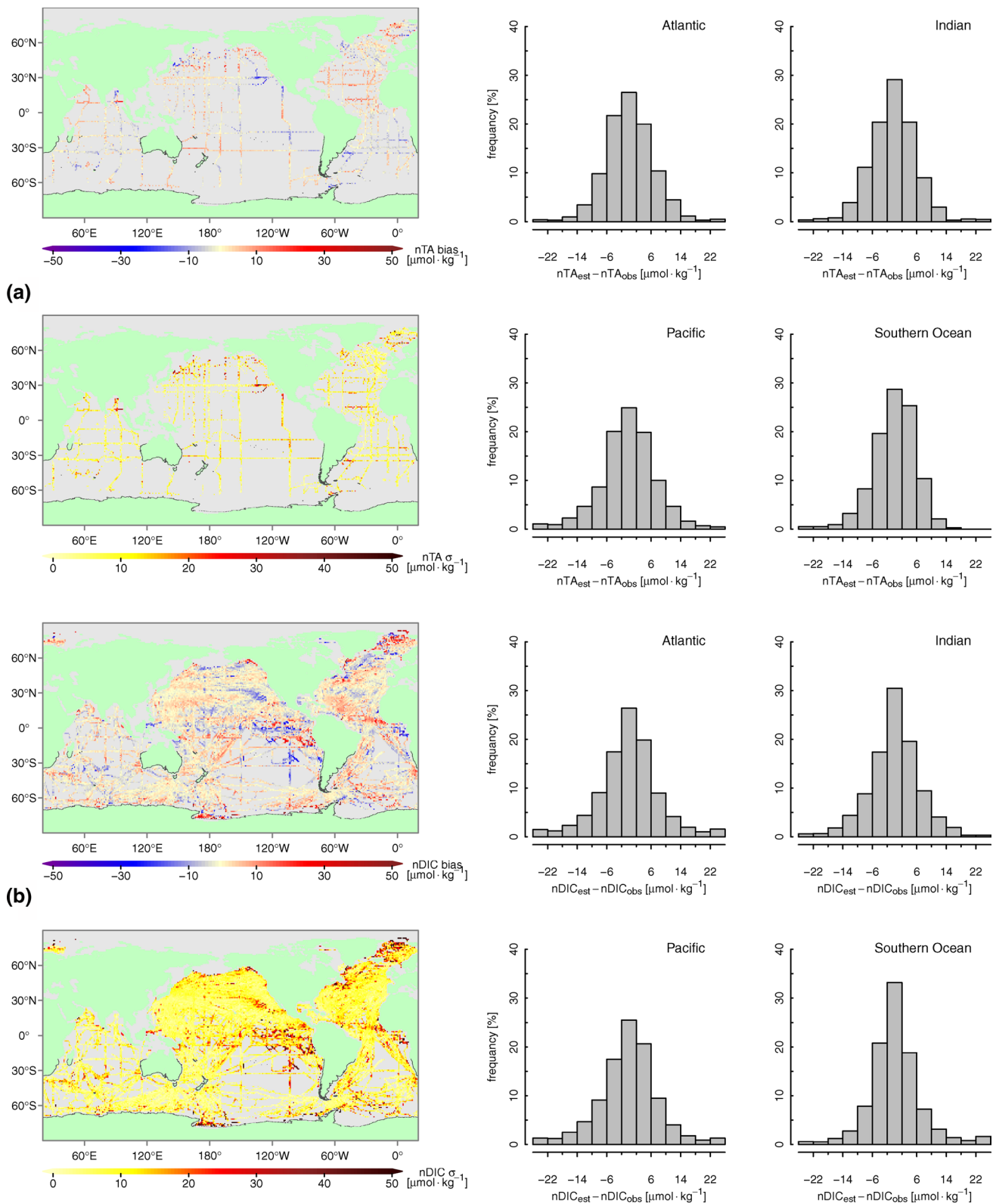


Fig. 4 Distributions of climatological biases and median absolute errors (left) and histograms of differences between observations and estimates (right) for **a** nTA and **b** nDIC. Map areas where no data are available are colored gray (color figure online)

Table 2 Biases and σ 's associated with estimates of nDIC, $p\text{CO}_2\text{sea}$, pH, and Ω_{arg}

		nDIC [$\mu\text{mol kg}^{-1}$]		$p\text{CO}_2$ [μatm]		pH		Ω_{arg}	
		Bias	σ	Bias	σ	Bias	σ	Bias	σ
Reproducibility	Regression	+0.1	6.1	+0.2	10.9	-0.000	0.011	-0.00	0.06
	Total	-0.1	8.2	-0.3	12.1	+0.001	0.012	-0.00	0.08
Subsampling validation	Regression	+0.1	5.9	+0.2	10.8	-0.000	0.011	-0.00	0.06
	Total	-0.1	8.0	-0.4	11.9	+0.001	0.012	-0.00	0.08
Independent validation	Regression	+0.6	11.2	-1.4	18.6	+0.002	0.019	+0.01	0.11
	Total	-1.9	11.5	-4.0	17.8	+0.004	0.018	+0.03	0.11

with other empirical methods, e.g., 14.4 μatm (Landschützer et al. 2014) and 15.73 μatm (Denvil-Sommer et al. 2019). The σ for nDIC based on a comparison with the independent data of GLODAPv2.2019 was 11.5 $\mu\text{mol kg}^{-1}$, which is larger than the σ of 6.1 $\mu\text{mol kg}^{-1}$ noted above.

3.1.2 Assessment of uncertainty of CO₂ uptake

Uncertainty in the calculation of the globally integrated sea-air CO₂ flux from Eq. 3 originates from the estimation of the difference in $p\text{CO}_2$ between the sea and air ($\Delta p\text{CO}_2$) and the gas exchange coefficient (Wanninkhof 2014). First, we assessed the uncertainty in $\Delta p\text{CO}_2$ following the method of Watson et al. (2009) and Landschützer et al. (2014). If the uncertainty of $\Delta p\text{CO}_2$ originates mainly from processes involved in the estimation of $p\text{CO}_2\text{sea}$ via MLRs and not from measurements of $p\text{CO}_2\text{sea}$ and $p\text{CO}_2\text{air}$, the uncertainty of $\Delta p\text{CO}_2$ on a basin scale can be expressed by superposition of the uncertainties of the $p\text{CO}_2\text{sea}$ gridded to $1^\circ \times 1^\circ$ squares and the uncertainties associated with mapping $p\text{CO}_2\text{sea}$ through the estimation process (Eq. 7) modified from Eqs. 1 and 2 of Landschützer et al. (2014).

$$\begin{aligned} \text{var}(\langle \Delta p\text{CO}_2\text{sea} \rangle_{\text{basin}}) &= \text{var}(\langle p\text{CO}_2\text{sea} \rangle_{\text{basin}})_{\text{grid}} + \text{var}(\langle p\text{CO}_2\text{sea} \rangle_{\text{basin}})_{\text{map}} \\ &= \frac{\text{var}(p\text{CO}_2\text{sea})_{\text{grid}}}{N_{\text{grid}}^{\text{eff}}} + \frac{\text{var}(p\text{CO}_2\text{sea})_{\text{map}}}{N_{\text{map}}^{\text{eff}}}, \end{aligned} \quad (7)$$

where $\text{var}(\langle p\text{CO}_2\text{sea} \rangle_{\text{basin}})_{\text{grid}}$ and $\text{var}(\langle p\text{CO}_2\text{sea} \rangle_{\text{basin}})_{\text{map}}$ indicate basin scale variances associated with processes gridding $p\text{CO}_2\text{sea}$ to $1^\circ \times 1^\circ$ squares and estimating $p\text{CO}_2\text{sea}$, respectively, and $N_{\text{grid}}^{\text{eff}}$ and $N_{\text{map}}^{\text{eff}}$ represent effective degrees of freedom of the respective processes. In Landschützer et al. (2014), the σ from gridding $p\text{CO}_2$ measurements was assumed to be 5 μatm based on an estimate of Sabine et al. (2013), and $N_{\text{grid}}^{\text{eff}}$ was estimated to be the total area divided by the square of the global mean autocorrelation length for $p\text{CO}_2\text{sea}$ (400 km^2 ; Jones et al. 2012). The first term in Eq. 7 generated mostly smaller values than the second term, and thus we ignored it and

focused on $\text{var}(\langle p\text{CO}_2\text{sea} \rangle_{\text{basin}})_{\text{map}}$, which is related to the $p\text{CO}_2\text{sea}$ estimation process. To estimate the variance, we set nine basins integrated from 57 subzones and derived $\text{var}(\langle p\text{CO}_2\text{sea} \rangle_{\text{basin}})_{\text{map}}$ for those basins. The $\text{var}(\langle p\text{CO}_2\text{sea} \rangle_{\text{map}})$ was obtained from the square of the σ discussed in Sect. 3.1.1, and $N_{\text{map}}^{\text{eff}}$ was estimated from the total area and the autocorrelation length of $p\text{CO}_2$ estimation residuals obtained from the semivariograms in each basin. Autocorrelation lengths were derived from semivariograms of the variances in the nine basins. This procedure generated basin scale $\sigma = \sqrt{\text{var}(\langle p\text{CO}_2\text{sea} \rangle_{\text{basin}})_{\text{map}}}$ that ranged from 1.0 to 5.0 μatm and CO₂ fluxes that ranged from 0.01 to 0.08 PgC year^{-1} when the mean sensitivity of $\Delta p\text{CO}_2$ to flux and the total basin area were multiplied. A globally integrated σ of the CO₂ flux calculated from the $\Delta p\text{CO}_2$ estimate of 0.28 PgC year^{-1} was obtained in this way. The value was slightly larger than the value of 0.17 PgC year^{-1} obtained by Landschützer et al. (2014). Our value accounted for 14% of the mean global oceanic CO₂ uptake of -1.98 PgC year^{-1} in 1993–2018. In addition, there is uncertainty in the gas transfer coefficient, k , in Eq. 3 because of the uncertainties in a , U_{10} , and Sc in Eq. 4: its overall σ has been estimated to

be around 20% (Wanninkhof et al. 2014). This uncertainty combined with the σ from $\Delta p\text{CO}_2$ mentioned above gives a σ for global oceanic CO₂ uptake of 0.49 PgC year^{-1} , i.e., 25% of the total uptake.

3.2 Trends of global and basin scale CO₂ uptake and ocean acidification

Despite the monotonic increase of anthropogenic CO₂ emissions during previous decades, the ocean CO₂ uptake evaluated in this study has shown decadal variability, i.e., stagnation during the 1990s and an increase after 2000

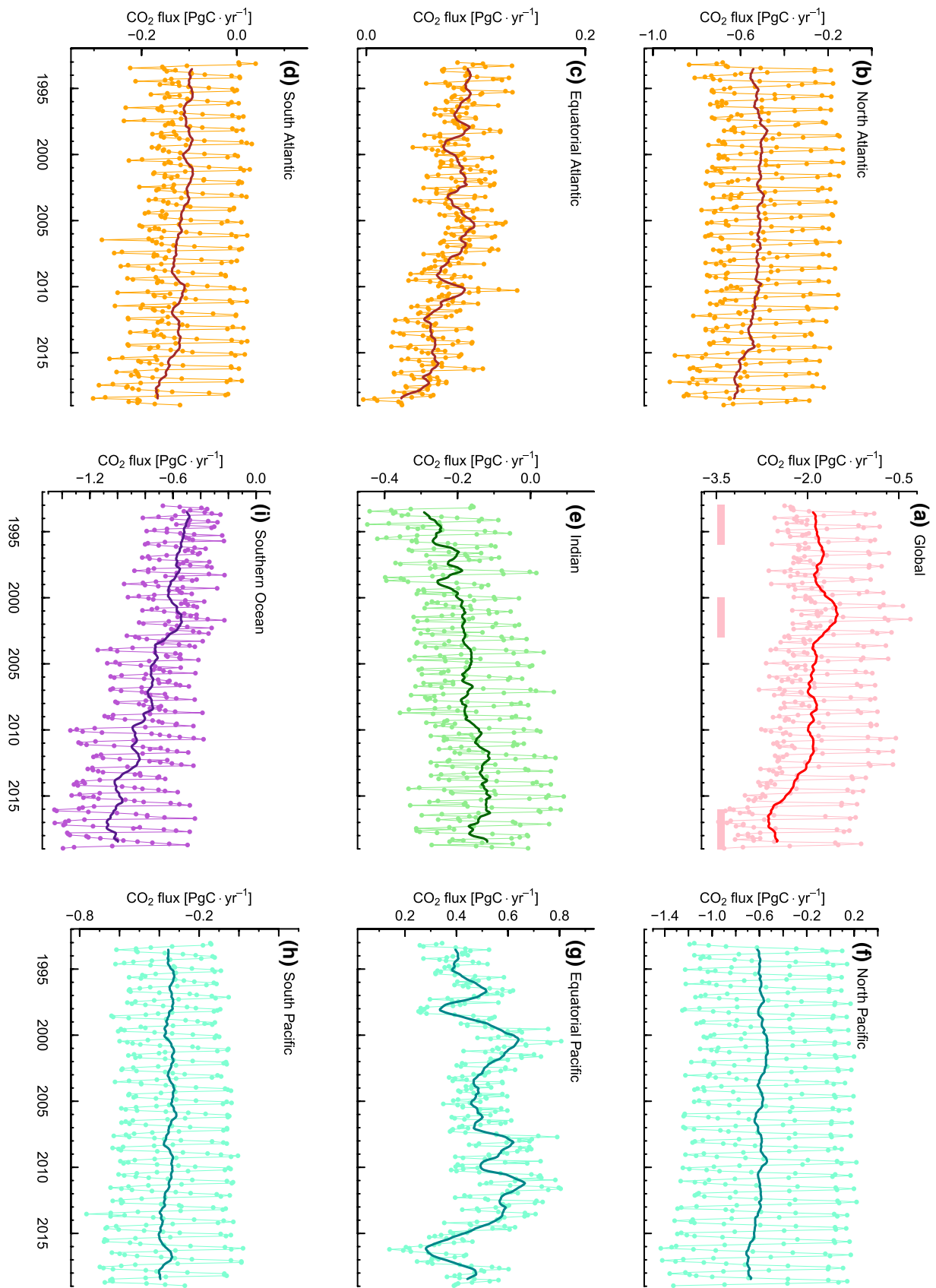


Fig. 5 Time-series representation of monthly sea-air CO₂ fluxes in the basins. Fluxes are corrected to yearly values. A positive/negative value indicates a source/sink for atmospheric CO₂. Thin and thick lines show monthly and one-year running mean fluxes, respectively. Horizontal lines at the bottom of panel **a** indicate the time intervals 1993–1995, 2000–2002, and 2016–2018

(Fig. 5a). These trends have also been pointed out by Iida et al. (2015) and in other observation-based studies (Rödenbeck et al. 2015). Three-year mean rates of ocean CO₂ uptake were -1.87 ± 0.05 PgC year⁻¹ for 1993–1995, -1.59 ± 0.08 PgC year⁻¹ for 2000–2002, and -2.59 ± 0.07 PgC year⁻¹ for 2016–2018. Note that the values calculated here are contemporary fluxes, and addition of the riverine flux is necessary to derive anthropogenic components. Rates of change of the CO₂ uptake in each ocean basin (Table 3) show that the decrease of the uptake in the 1990s was predominantly (> 80%) attributable to a decrease in the Pacific Ocean, particularly in the tropical Pacific because of the increase of CO₂ emissions from the equatorial divergence zone. In contrast, the increase of CO₂ uptake after 2000 is attributable mainly to an increase in the Southern Ocean (~40%) and Pacific Ocean (~40%) and to a lesser extent in the Atlantic Ocean (~20%). The Southern Ocean did not contribute to the decreased uptake during the 1990s, but the time-series (Fig. 5i) showed a stagnation of uptake during the 1990s and reinvigoration after 2000 that were similar to the patterns in the other basins. Overall, the annual global ocean CO₂ uptake increased at a mean rate of -0.30 ± 0.05 (PgC year⁻¹) decade⁻¹ for the period of 1993–2018. This estimate agrees well with the mean rate of -0.33 ± 0.02 (PgC year⁻¹) decade⁻¹ assessed by an ensemble of global ocean biogeochemical models for the same period (Friedlingstein et al. 2019).

Global and basin scale mean trends for pH and Ω_{arg} were also evaluated from the gridded data produced in this work. Time-series of pH and Ω_{arg} anomalies integrated over the global open ocean showed that their mean rates of change were -0.0181 ± 0.0001 and -0.082 ± 0.001 decade⁻¹, respectively (Fig. 6). These rates are comparable with the rates that have been reported from the Hawaii Ocean Time-series (HOT) in the North Pacific, Bermuda Atlantic Time-series Study (BATS), and European Station for Time-series in the Ocean, Canary Islands (ESTOC) in the North Atlantic (Bates et al. 2014), and 137° E section in the western North Pacific (P9: Ono et al. 2019). They are also consistent with the rate expected when surface seawater maintains a transient equilibrium with the growth of atmospheric CO₂. A large portion of the ocean surface layer exhibited rates of pH decrease similar to those expected from the increase of atmospheric CO₂ (Fig. 7a), whereas slower rates of pH change of -0.0148 ± 0.0002 to -0.0165 ± 0.001 decade⁻¹, drawn with cold colors in Fig. 7a, were also seen in some regions, such as offshore of western North America in the

eastern North Pacific, in the western Pacific tropical zone, in the Angola-Benguela system in the South Atlantic, and in the Southern Ocean (Fig. 7a–d). All these regions are proximate to regions where the upward transport of anthropogenic CO₂ from subsurface waters via overturning circulation has been identified with Lagrangian diagnostic of a climatological ocean carbon cycle model (Toyama et al. 2017).

4 Discussion and summary

Observation-based diagnostic models of $p\text{CO}_2\text{sea}$ tend to show larger decadal variability of ocean CO₂ uptake than that simulated by ocean biogeochemistry models (DeVries et al. 2019). The results of this study indicate that CO₂ uptake decreased during the 1990s and has been increasing since 2000 (Fig. 5). Similar patterns have been reported in previous observation-based studies (Rödenbeck et al. 2015), especially in the Southern Ocean (Landschützer et al. 2015; Ritter et al. 2017; Gruber et al. 2019b). These studies have shown that the intensification of the CO₂ sink in the Southern Ocean from the early 2000s to around 2010 was induced by a thermal decrease of the $p\text{CO}_2\text{sea}$ due to cooling in the Pacific sector and non-thermal decreases resulted from weakening of the vertical mixing in the Atlantic and Indian Ocean. DeVries et al. (2017) have argued on the basis of an ocean inverse model that was constrained by ocean interior measurements that the decrease of CO₂ uptake in the 1990s and the increase after 2000 in the Southern Ocean were caused by changes in the natural CO₂ release to the atmosphere associated with a strengthened meridional overturning circulation in the 1990s and a decline of that circulation in the 2000s, especially in the Atlantic and Indian sectors. In this study, 40% of the increase in CO₂ uptake after the 2000s in the Southern Ocean resulted from its northern parts of the Pacific, Atlantic, and Indian Ocean sectors (not shown), and there was also an increase of uptake in the South Atlantic during that time (Fig. 5d), supporting some of the conclusions of DeVries et al. (2017).

To investigate factors controlling the variability of CO₂ uptake over the Southern Ocean, we first evaluated the contributions of the variability of SST, SSS, nDIC, and nTA to the yearly $p\text{CO}_2\text{sea}$ anomaly over the Southern Ocean and then the contribution of each explanatory variable in the MLRs to the yearly nDIC anomaly (Fig. 8). The physicochemical contributions of SST, SSS, nDIC, and nTA were calculated from their anomalies (differences from monthly climatology) and their sensitivities to the $p\text{CO}_2\text{sea}$ variation based on the carbonate chemistry. The contributions of MLR variables were calculated from differences between the nDICs derived from ordinary explanatory variables and ones derived using climatological values of specific explanatory variables. In the context of thermodynamic components, the variability

Table 3 Three-year mean CO₂ uptake during (a) 1993–1995, (b) 2000–2002, and (c) 2016–2018 and contributions (%) to global (1) decrease from period (a) to period (b) and (2) increase from period (b) to period (c). Positive values indicate uptake from the atmosphere

	(a) 1993–1995 [PgC year ⁻¹]	(b) 2000–2002 [PgC year ⁻¹]	(c) 2016–2018 [PgC year ⁻¹]	(1) Decrease (a) to (b) (%)	(2) Increase (b) to (c) (%)	Areas ^{*5} [10 ⁶ km ²]	
Global ^{*1}	+1.87	+1.59	+2.59	–	–	321	
Atlantic ^{*2}	18°N–	+0.54	+0.51	+0.61	10	10	
	18°S–18°N	–0.11	–0.10	–0.05	–3	5	
	44–18°S	+0.22	+0.23	+0.32	–2	9	
	Total	+0.65	+0.64	+0.88	5	24	71
Indian ^{*3}	18°S–	–0.08	–0.14	–0.15	19	–2	
	44–18°S	+0.51	+0.47	+0.47	13	–1	
	Total	+0.42	+0.34	+0.31	32	–2	50
Pacific ^{*4}	18°N–	+0.56	+0.51	+0.62	18	12	
	18°S–18°N	–0.32	–0.52	–0.27	71	24	
	44–18°S	+0.45	+0.46	+0.51	–1	5	
	Total	+0.69	+0.45	+0.86	87	41	140
Southern Ocean	–44°S	+0.10	+0.16	+0.54	–24	38	61

^{*1}The coastal areas, defined to be the pixels next to the land, and some marginal seas listed in ^{*2–4} are excluded from the analysis. The flux associated with these excluded areas is estimated to be around -0.25 PgC year⁻¹ based on the climatological $p\text{CO}_2\text{sea}$ data of Landschützer et al. (2020), $p\text{CO}_2\text{air}$ and gas exchange coefficients in this study

^{*2}The Mediterranean, Black Sea, Baltic Sea, and Arctic Archipelago are excluded

^{*3}The Persian Sea and the Red Sea are excluded

^{*4}The Pacific side of Arctic Ocean, the Bering Sea, and East Asian marginal seas except for the East China Sea, are excluded

^{*5}The total area analysed is smaller than that of the global ocean, which is about 360×10^6 km²

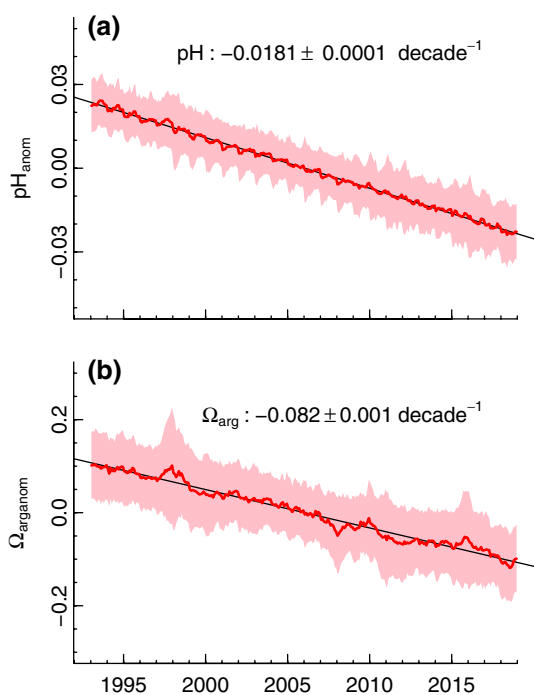


Fig. 6 Time-series representation of anomalies of pH and Ω_{arg} . Thick lines indicate mean anomalies of pH and Ω_{arg} , and the shading indicates standard deviations. Thin black lines show long-term trends of pH and Ω_{arg} decreases. The numbers are the rates of change \pm standard errors

in $p\text{CO}_2\text{sea}$ is mainly ascribed to the variability of nDIC, followed by that of SST with minor contributions from the variability of SSS and nTA (Fig. 8b). The increase/decrease in nDIC is ascribed to the SST drop/rise in the MLR method because of the negative correlation between them. We found an increase of the magnitude of the negative anomaly of $p\text{CO}_2\text{sea}$ (a change of anomaly from positive toward negative) especially after late 2000s (Fig. 8a/b). In the Indian sector, an increase in negative nDIC anomaly occurred during the period from mid 2000s to 2011. Such change occurred in the Atlantic sector from early 2000s and in the Pacific sector after 2012 (Fig. 8a1–4). The fact that the increase of the negative anomaly of $p\text{CO}_2\text{sea}$ is ascribed to the nDIC decrease that was associated with the SST rise probably reflects the results of stratification in these regions. An increase of Chl concentrations at high latitudes in the Southern Ocean also contributed to the decrease in nDIC. Thermodynamically, the effect of the nDIC decrease exceeded the effect of the temperature rise. The resultant lowering of $p\text{CO}_2\text{sea}$ (Fig. 8b) led to the increase of CO₂ uptake after 2000. The results of the present study are consistent with the patterns described in previous studies (Landschützer et al. 2015; DeVries et al. 2017; Ritter et al. 2017; Gruber et al. 2019b). In addition, this study indicated that the increase of CO₂ uptake has continued into the 2010s and has occurred mainly in the Pacific sector of the Southern Ocean.

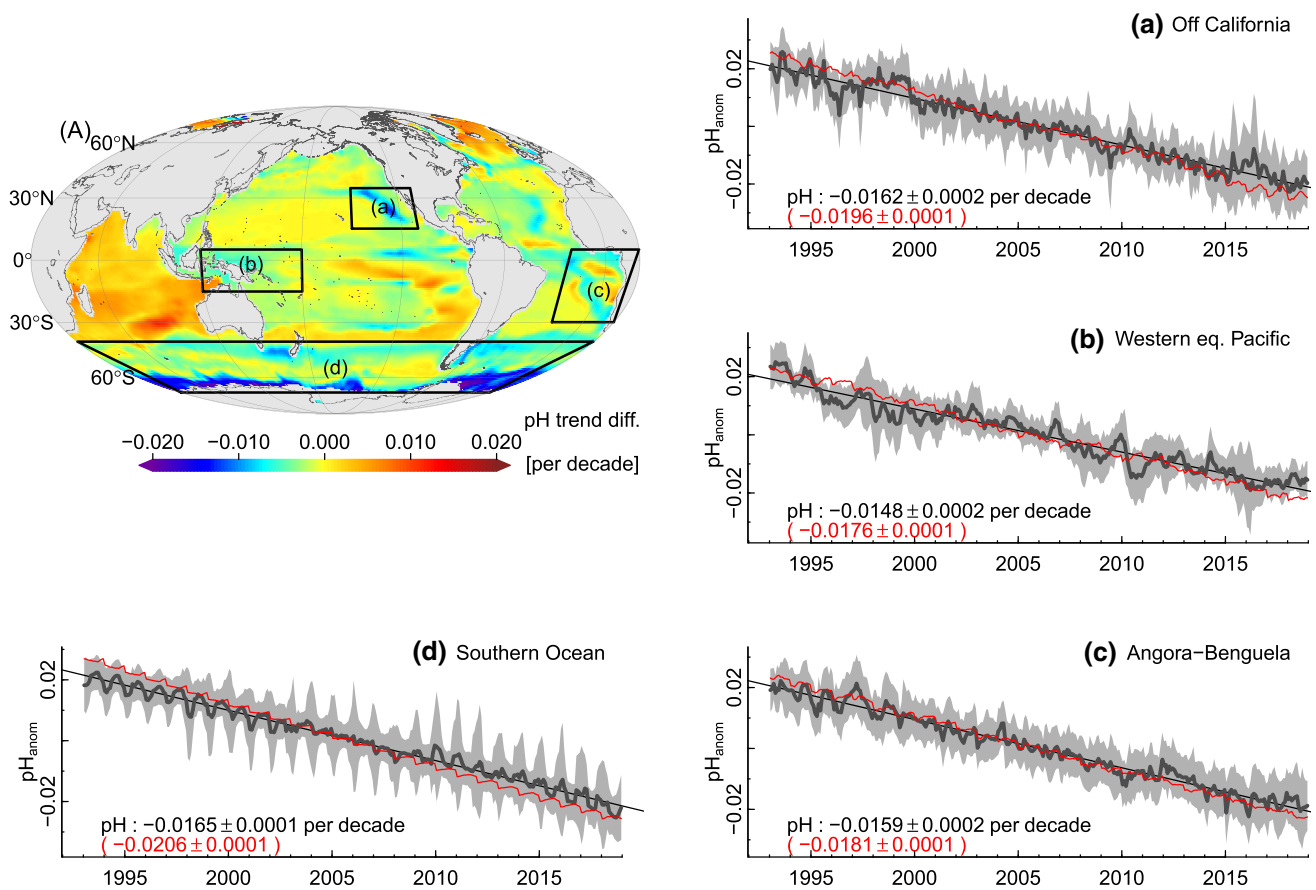


Fig. 7 **a** The distribution of differences between trends of pH anomalies and trends of atmospheric CO₂-induced pH anomalies, and **a–d** time-series representations of pH anomalies and atmospheric CO₂-induced pH anomalies. Thick lines indicate monthly pH anomalies, and the gray shading indicates standard deviations.

Red lines show monthly atmospheric CO₂-induced pH anomalies. Thin black lines show long-term trends of decrease. The numbers are trends ± standard errors and correspond to pH anomalies (black numbers) and atmospheric CO₂-induced pH anomalies (red numbers) (color figure online)

DeVries et al. (2017) have also concluded that CO₂ uptake increased in the Indian Ocean during the 2000s. However, the results of this study indicate that the CO₂ sink of the Indian Ocean was decreasing in the 2000s (Fig. 5e). This inconsistency could be ascribed to the potential bias in the secular trend of DIC. The secular trend in the Indian Ocean estimated in this study depended on data from the equatorial region because of the paucity of data from the northern Indian Ocean.

The CO₂ source in the equatorial Pacific was the smallest around the year 2016 because of the strong El Niño at that time and contributed to the increase of the ocean CO₂ sink after 2010. The CO₂ source in the equatorial Pacific strengthened after 2016 with the cessation of El Niño and contributed to the weakening of the global ocean CO₂ sink during that period (Fig. 5a, g).

Our analysis did not reveal synchrony of the decadal variability of pH and Ω_{arg} with ocean CO₂ uptake (Fig. 6). We did not find that the decreases of pH and Ω_{arg} were smaller before 2000 and larger after 2000. The estimated global

mean pH and Ω_{arg} were respectively 8.10 and 3.06 in 1993, 8.08 and 2.96 in 2005, and 8.06 and 2.87 in 2018. The mean rates of changes were -0.018 and -0.082 decade⁻¹ for pH and Ω_{arg} , respectively. If we assume that the rate of change of the pH anomaly, -0.018 decade⁻¹, continues in the near future, the global mean pH is very likely to reach 8.05 in 2023. In other words, after 2023 the global mean pH will be 8.0 rounded to two significant figures, not the often-cited pH of 8.1 (e.g., IPCC 2013). Aside from the equatorial Pacific, where pH and Ω_{arg} vary substantially along with the El Niño Southern Oscillation, interannual and decadal variability of the anomalies of pH and Ω_{arg} were obscure when they were integrated over a basin (Figs. 6; 7a–d). The trend in pH that we identified in this study was consistent with those from time-series observations (Bates et al. 2014) and the Copernicus Marine Environmental Monitoring Service (CMEMS) estimates of global pH (<https://marine.copernicus.eu/science-learning/ocean-monitoring-indicators>) calculated from the TA reported by Carter et al. (2018) and the $p\text{CO}_2$ sea reported by Denvil-Sommer et al. (2019). The rate of pH

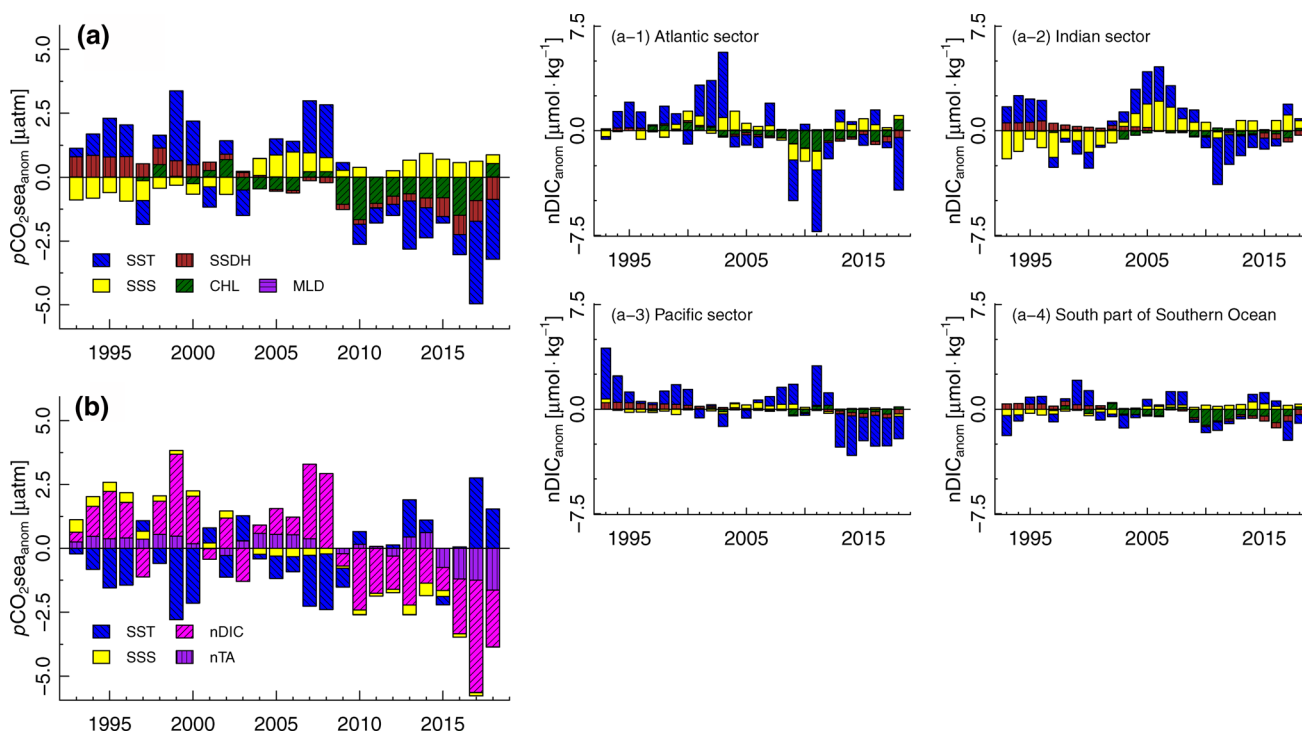


Fig. 8 The contributions from variables to the yearly $p\text{CO}_2\text{sea}$ anomaly. **a** Shows the contributions of the explanatory variables in the MLR over the Southern Ocean. Panels a-1, a-2, and a-3 correspond to the Atlantic, Indian, and Pacific sectors of the northern part of South-

ern Ocean, respectively, and a-4 corresponds to the southernmost part of the Southern Ocean, showing the contributions to nDIC anomaly. **b** Shows the contributions from physicochemical effects of temperature, salinity, nDIC, and nTA over the Southern Ocean

change estimated by CMEMS was -0.0016-year^{-1} during the period of 1985–2018. As mentioned in Sect. 3.2, the magnitude of the rate of pH decrease was lower in some regions, such as the Southern Ocean, western equatorial Pacific, and eastern boundary current regions off California and the Angora-Benguela system. Although the reasons for the slower acidification in those areas are unclear, the slower rate of acidification in the western tropical Pacific is consistent with the slower pH decrease in the tropical area near the 137°E meridian ($-0.0124 \pm 0.0008\text{ decade}^{-1}$, Ono et al. 2019).

Finally, SDG 14.3 addresses ocean acidification, and the indicator of ocean acidification defined in SDG 14.3.1 requires “Average marine acidity (pH) measured at agreed suite of representative sampling stations”. This definition is based on surface ocean pH “measured directly or can be calculated based on data for two of the other carbonate chemistry parameters, these being TA, DIC and $p\text{CO}_2$.” (IOC/UNESCO 2018). However, measurements are not always sufficient in space and time to assess representative values of pH for each region, and thus the average pH calculated from the reconstructions proposed in this study could help verifying a value of the indicator (Wanninkhof et al. 2019).

Acknowledgements Gridded data of inorganic carbon variables and ocean CO_2 uptake calculated in this study are available at the JMA web site: https://www.data.jma.go.jp/gmd/kaiyou/english/co2_flux/co2_flux_data_en.html. The Surface Ocean CO_2 Atlas (SOCAT) is an international effort, endorsed by the International Ocean Carbon Coordination Project (IOCCP), the Surface Ocean Lower Atmosphere Study (SOLAS) and the Integrated Marine Biosphere Research (IMBeR) program, to deliver a uniformly quality-controlled surface ocean CO_2 database. SOCAT data sets are available at <https://www.socat.info>. We thank the many researchers and funding agencies responsible for the collection of data and quality control for their contributions to SOCAT. Data of GLODAPv2 are also available at <https://www.nodc.noaa.gov/ocads/oceans/GLODAPv2/>. We also thank the GLODAP v2 team and data originators. GlobColour data (<https://globcolour.info>) used in this study have been developed, validated, and distributed by ACRI-ST, France. The altimeter products were produced by Ssalto/Duacs and distributed by Aviso+, with support from Cnes (<https://www.aviso.altimetry.fr>). This study was supported by MRI’s research fund C4 for the studies of ocean biogeochemistry and ocean acidification.

Appendix 1: Derivation of equations to estimate surface ocean TA

Here we describe processes used to derive surface ocean TA from SSS and SSDH by using MLR in accord with the method of Takatani et al. (2014). As described in Takatani et al. (2014), there is a distinct negative correlation between

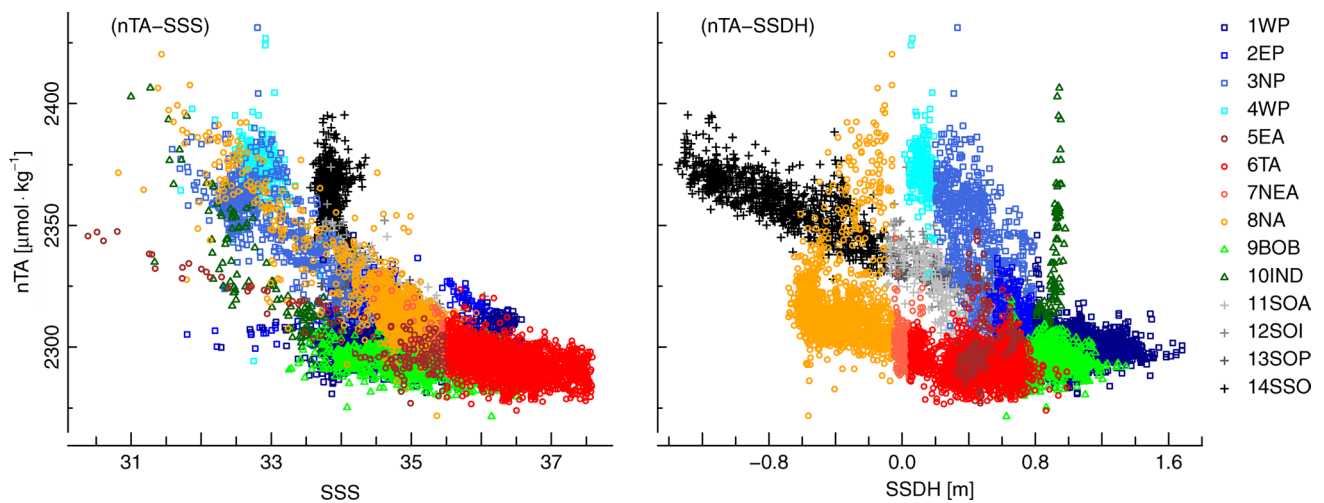


Fig. 9 Relationships of nTA versus **a** SSS and **b** SSDH in the global ocean. Plots are colored by zone. Abbreviations of zone names are defined in the text

nTA and SSDH, with the exception of some scattered data in a narrow SSDH range that reflect SSS variations (Fig. 9). We therefore used SSS and SSDH as explanatory variables in the MLR.

$$\text{nTA} = f(\text{SSS}, \text{SSDH}). \quad (8)$$

We used definitions of zones that were similar but slightly modified from the definitions used by Takatani et al. (2014) for the Pacific Ocean as follows. (1) The high SSDH area ($\text{SSDH} > 0.8$ m) was classified as zone 1WP. This zone represented the northern and southern subtropical gyres and the western equatorial warm pool. The nTAs show a nearly constant value of $\sim 2300 \mu\text{mol} \cdot \text{kg}^{-1}$ because few processes that change nTA occur in this area. (2) The area characterized by SSDHs of 0.2–0.8 m south of the salinity maximum around 25° N was assigned to zone 2EP, whereas the method of Takatani et al (2014) divided this area meridionally along 120° W. This zone represents upwelling areas of the eastern equatorials, off Peru and off Costa Rica. The higher nTAs in 2EP than in 1WP reflect the high nTA of upwelled seawater. (3) The area characterized by SSDHs of 0.2–0.8 m north of the salinity maximum represents the subtropical-subarctic transition and was named 3NP. This zone is characterized by seawater with a wide range of SSSs, from ~ 35 , which is representative of subtropical seawater, to around 32–33, which is representative of subarctic seawater. The regression explanatory variables therefore included SSS. (4) The area characterized by SSDHs less than 0.2 m was assigned to the North Pacific subarctic gyre (4WSAG) and was characterized by a high and nearly constant value of nTA.

An approach similar to that used in the Pacific was applied to the Atlantic. First, an equatorial area characterized by $\text{SSS} < 35.5$ due to the influence of large rivers such

as the Amazon and Congo was designated zone 5EA. The area with $\text{SSDH} > 0.05$ m, which is representative of the tropical and subtropical Atlantic, was classified as 6TA. The use of SSS for zone 5EA could better account for the non-zero nTA source of the large rivers (Lefèvre et al. 2010). The nTA in 6TA was nearly constant and similar to the nTA of zone 1WP in the Pacific. The area characterized by $-0.2 > \text{SSDH} > 0.2$ m represented the subtropical-subarctic transition, and a northern area characterized by SSDHs less than 0.2 m represented the North Atlantic subarctic gyre; these two areas were classified as 7NEA and 8NA, respectively. In these four zones, SSS and/or SSDH were used for the regressions.

In the Indian Ocean, the Bay of Bengal (9BOB), where there is a large input of freshwater from the Ganges–Brahmaputra River, was distinguished from the rest of the Indian Ocean (10IND) by $\text{SSS} < 34$. The SSS in 9BOB was used to correct the nTA in 9BOB for the influence of the riverine input of nTA (Bates et al. 2006) in the same way that SSS was used to correct the nTA in 5EA in the Atlantic. The nTA in 10IND was nearly constant, despite the inclusion of observations during the southwestern monsoon season, which could have affected the carbonate system in this zone (Sreesh et al. 2019).

The Southern Ocean was distinguished by $\text{SSDH} < 0.05$ m from the Atlantic, by $\text{SSDH} < 0.65$ m from the Indian, and by $\text{SSDH} < -0.8$ m from the Pacific. Midorikawa et al. (2012) used the 5°C SST isotherm as a proxy for the subarctic front to estimate TA. In this study, the northern and southern parts of the Southern Ocean were distinguished by $\text{SSDH} = -0.1$ m as a proxy for the frontal area, and the northern was further divided into three ocean sectors (11SOA, 12SOI, 13SOP, and 14SSO). In these zones, both SSDH and SSS ranged widely and were used as MLR variables.

Table 4 Zone and subzone definitions used to estimate nTA and nDIC. Abbreviations of zones and subzones can be found in the text

	nTA	nDIC	
<i>Pacific</i>			
1WP	SSDH \geq 0.8 m	1NWP	Lat \geq N.SSDHmin ^a
		2SWP	Lat $<$ S.SSDHmin ^b
		3WEQ	S.SSDHmin $<$ Lat $<$ N.SSDHmin & SSS $<$ 34.7 & SST \geq 27
		4CEQ	S.SSDHmin $<$ Lat $<$ N.SSDHmin & (SSS \geq 34.7 or SST $<$ 27)
		2EP	25°S \leq Lat $<$ SSSmax ^c & 0.2 m \leq SSDH $<$ 0.8 m
3NP	Lat \geq SSSmax & 0.2 m \leq SSDH $<$ 0.8 m	1PERU	Lat $<$ 15°S
		2EPFP	SSS $<$ 34
		3EEQ	SSS \geq 34
		4COS	Lon \geq 105°W & SSDH $<$ 0.7
		5NEEQ	not assigned to the others
		1NSBT	SST \geq 16 & Lon $<$ SSDHmax ^d
		2CAL	SST \geq 16 & Lon $>$ SSDHmax
		3STR	Winter ¹ 5 \leq SST $<$ 16 & SSDH \geq 0.35 Summer ²
		4SRK	Winter 5 \leq SST $<$ 16 & SSDH $<$ 0.35 & SSS $>$ 33.3 Summer
		5ESBA	Winter 5 \leq SST $<$ 16 & SSDH $<$ 0.35 & SSS $<$ 33.3 Summer
6NSBA	Winter SST $<$ 5 Summer	1w	Winter (all)
		2LTs	Summer SST $<$ 7.5
		3HTs	SST \geq 7.5
4WSAG	Lat $<$ 25°S & SSDH \leq 0.2 m		
<i>Atlantic</i>			
5EA	20°S \leq Lat \leq 30°N & SSS $<$ 35.5	1LS	(all)
6TA	Lat \geq 30°N & SSDH \geq 0.05 m & SSS \geq 35.5 or 20°S \leq Lat. \leq 30°N & SSS \geq 35.5 or Lat. \leq 20°S & SSDH \geq 0.05 m & SSS \geq 35.5	1NSBT	SSDH \geq 0.4 & Lat \geq N.SSDHmin ^e
		2SSBT	SSDH $>$ 0.4 & Lat $<$ S.SSDHmin ^f
		3WEQ	SSDH $>$ 0.4 & S.SSDHmin $<$ Lat $<$ N.SSDHmin
		4ABR	SSDH $<$ 0.4 & Lat $<$ S.SSDHmax ^g
		5EEQ	SSDH \geq 0.4 & S.SSDHmax $<$ Lat $<$ eqSSDHmax ^h
		6GST	SSDH $<$ 0.4 & Lon $<$ 60 W
		7GUI	SSDH $<$ 0.4 & eqSSDHmax $<$ Lat $<$ N.SSDHmax ⁱ
		8NESBT	SSDH $<$ 0.4 & Lat \geq N.SSDHmax & SST $>$ 18
		9NSBT	SSDH $<$ 0.4 & Lat \geq N.SSDHmax & SST $<$ 18
		7NEA (-0.05 m \leq SSDH $<$ 0.05 m) or (SSDH \geq 0.05 m & SSS $<$ 35.5)	Lat. \geq 30°N & 1SSBA
2SESBA	Winter ³ SST $<$ 18 Summer ⁴		
8NA	Lat \geq 30°N & SSDH $<$ -0.05 m	1GLB	Winter SSS $<$ 34.3 Summer

Table 4 (continued)

	nTA	nDIC	
		2ESBA	Winter SSS \geq 34.3 & SST > 7.8 Summer
		3NSBA	Winter SSS > 34.3 & SST < 7.8 Summer
<i>Indian</i>			
9BOB	Lat \geq 0°N & SSS < 34.3	11BOB	all
10IND	Lat \geq 25°S except 9BOB or Lat < 25°S & SSDH \geq 0.65 m	1AREX	Lat \geq SSDHmin ^j & SSS \geq 35.3 & SST \geq 28.3
		2ARnsw	Oct–May Lat \geq SSDHmin & SSS \geq 35.3 & SST < 28.3
		2ARsw1	Jun–Sep Lat \geq SSDHmin & SSS \geq 35.3 & SST < 27
		2ARsw2	Jun–Sep Lat \geq SSDHmin & SSS \geq 35.3 & 27 \leq SST < 28.3
		3EQ	(Lat \geq SSDH min & SSS < 35.3) or (SSDH max ^k < Lat < SSDH min & SSDH < 0.85)
		4WSBT	Lat < SSDH min & SSDH \geq 0.85
		5ESBT	Lat < SSDH max & SSDH < 0.85
<i>Southern Ocean</i>			
11SOA	Atlantic Lat. \leq 20°S & SSDH \leq 0.05 m or SSS \leq 35.5	1SSBT	SST \geq 16
		2	Winter ⁵ SST < 16 & SSDH > 0.3 Summer ⁶
		3	Winter SST < 16 & 0.1 \leq SSDH < 0.3 Summer
		4	Winter SST < 16 & SSDH < 0.1 Summer
12SOI	Indian Lat. \leq 25°S & SSDH \leq 0.65 m	1SSBT	SST < 16 & SST > 16
		2	Winter SST < 16 & SSDH > 0.5 Summer
		3	Winter SST < 16 & 0.3 \leq SSDH < 0.5 Summer
		4	Winter SST < 16 & 0.1 \leq SSDH < 0.3 Summer
		5	Winter SST < 16 & SSDH < 0.1 Summer
13SOP	Pacific Lat. \leq 25°S & SSDH \leq 0.80 m	1SSBT	SST \geq 16
		2	Winter SST < 16 & SSDH > 0.5 Summer
		3	Winter SST < 16 & 0.3 \leq SSDH < 0.5 Summer
		4	Winter SST < 16 & 0.1 \leq SSDH < 0.3 Summer
		5	Winter SST < 16 & SSDH < 0.1 Summer
14SSO	SSDH \leq -0.10 m in southern hemisphere	1	Winter SSDH \geq -0.3 Summer
		2	Winter -0.5 \leq SSDH < -0.3 Summer
		3	Winter -0.7 \leq SSDH < -0.5 Summer
		4	Winter -0.9 \leq SSDH < -0.7

Table 4 (continued)

nTA	nDIC
	Summer
5	Winter $-1.1 \leq \text{SSDH} < -0.9$
	Summer
6	Winter $\text{SSDH} < -1.1$
	Summer

^aSSDH minimum along 5–10° N

^bSSDH minimum along 5° S

^cSSS maximum along 20–25° N

^dSSDH maximum around 140° W,

^eSSDH minimum along 10–15° N

^fSSDH minimum along 15–10° S

^gSSDH maximum along 8° S

^hSSDH maximum along 5° N

ⁱSSDH maximum along 20–25° N

^jSSDH minimum along 5° S

^kSSDH maximum along 30° S

¹ November to February

² March to October

³ November to February (October to February in area north of 67°N)

⁴ March to October (March to September in area north of 67°N)

⁵ May to September

⁶ October to April

Table 5 Regression coefficients for estimating nTA. Abbreviations of zones are defined in the text

TA zone	<i>a</i>	<i>b</i>	<i>c</i>	msss	σ	<i>N</i>
1WP	2300.3	–	–	35	5.0	1793
2EP	2356.2	–69.80	–	35	8.2	321
3NP	2387.3	–37.68	–21.38	32	9.5	677
4WSAG	2373.0	–	–	35	8.9	229
5EA	2302.6	35.84	–10.92	33	4.7	168
6TA	2294.1	–	–	35	6.3	2161
7NEA	2350.4	–	–18.90	33	4.7	246
8NA	2362.0	16.30	–22.59	33	5.8	1535
9BOB	2293.2	–	–33.08	34	11.1	124
10IND	2293.2	–	–	35	5.3	1136
11SOA	2318.8	–9.90	–18.73	35	5.0	276
12SOI	2323.5	–18.92	–16.41	35	1.7	376
13SOP	2319.4	–20.44	–16.53	35	4.4	695
14SSO	2336.1	–27.40	–23.57	34	6.2	879

The regression equation is $nTA = a + b \times \text{SSDH} + c \times \text{mSSS}$. In this equation, mSSS indicates SSS – msss, where msss is the representative salinity in each zone. Acronyms are defined in the text

Table 4 summarizes the definitions of zones and sub-zones, and the derived regression coefficients for each sub-zone are listed in Table 5.

Appendix 2: Derivation of equations to estimate surface ocean DIC

Here, we describe the derivation of the MLR equations used to estimate surface ocean DIC from SST, SSS, SSDH, Chl,

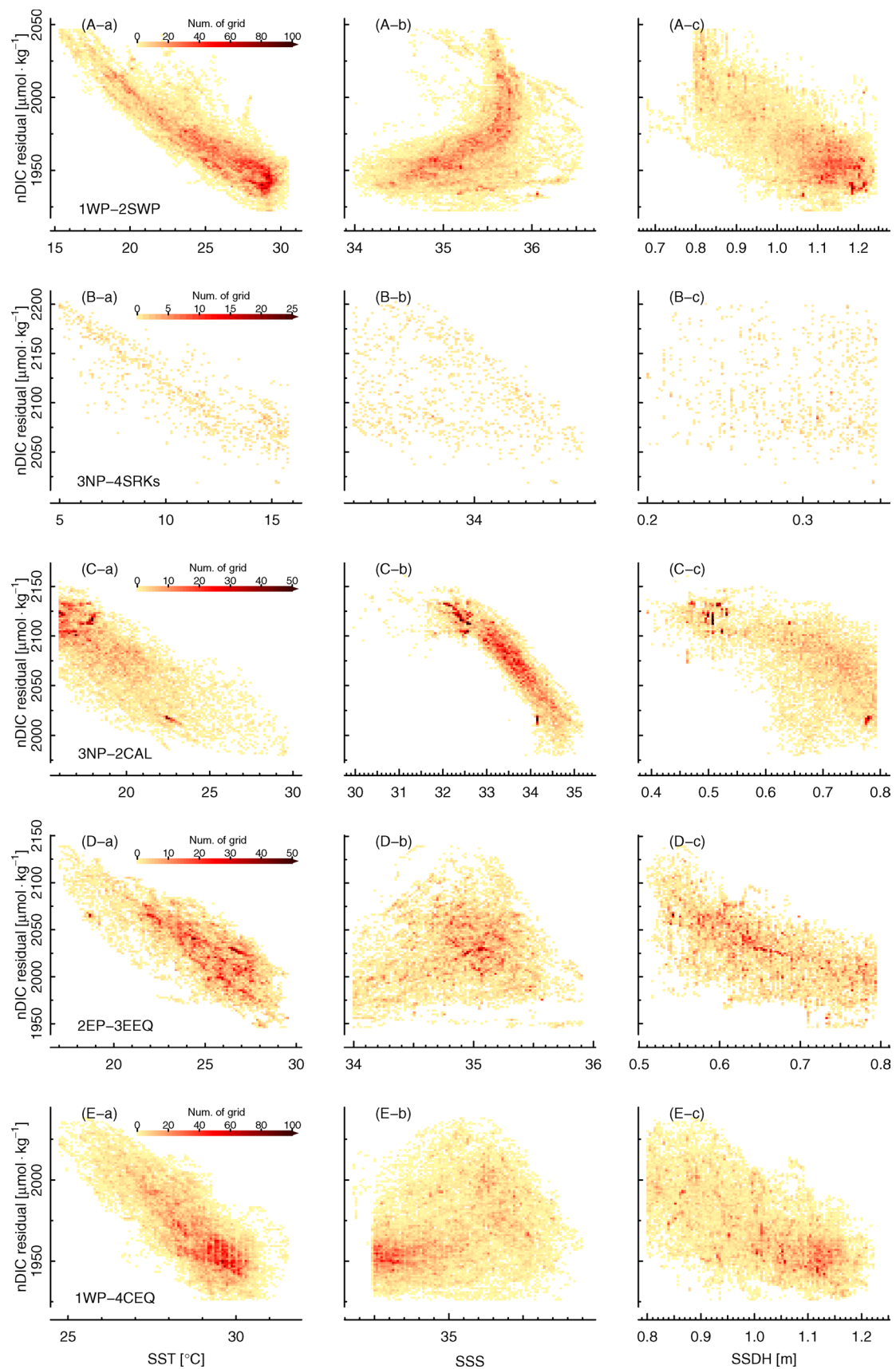


Fig. 10 Relationships of nDIC versus SST (left), SSS (center), or SSDH (right) in representative subzones of the Pacific Ocean. Coloring indicates the number of data in each grid. Abbreviations of subzone names are defined in the text

and MLD. We particularly emphasize the procedure for defining subzones.

Data procedure

We used SOCAT V2019 as a surface carbon dataset. Before conducting the MLR analysis, sub-hour data were binned to hourly data to eliminate possible bias from sampling frequency. Some records show unprecedented values of salinity during part or all of each cruise, probably because of equipment malfunction, and we excluded those records from the analysis. After that, $f\text{CO}_2$ data were converted to DIC in combination with the observed SST, SSS, the TA estimated from the observed SSS and satellite SSDH data, and climatological nutrients from the World Ocean Atlas 2018 (Garcia et al. 2018). To ignore DIC change resulted from simple fresh water flux, nDIC was used for MLR.

$$\text{nDIC} = f(\text{time, SST, SSS, SSDH, MLD, Chl}), \quad (9)$$

where the function f took a more general form than a simple MLR (vide infra). If a large number of explanatory variables are included in a MLR, the coefficients associated with some of the variables will be statistically insignificant. However, this statistical insignificance might not adversely affect the results if the MLR was applied within a limited area where the ranges of the variables were small.

In general, nDIC values were negatively correlated with SST, SSS, and SSDH over most of the ocean (Figs. 10, 11, 12 and 13). Based on the relationships in Figs. 10, 11, 12 and 13, we hypothesized that globally nDIC was a quadratic function of SST, SSS and SSDH. In a few subzones, the powers of the explanatory variables were tuned to avoid unlikely extrapolations. We assumed that the secular trends of nDIC were linear. In addition to SST, SSS, and SSDH, Chl and MLD were considered as additional variables based on the a priori hypothesis that Chl would be negatively correlated with nDIC because primary production would be expected to reduce nDIC, particularly from spring to autumn in subpolar subzones. Deepening of the mixed layer during the winter in subtropical and subpolar subzones would increase nDIC because of entrainment from lower seawaters. In some regions, the Chl concentrations were indeed negatively correlated with the nDIC residuals that remained after elimination of the variability associated with SST, SSS, and SSDH (Figs. 14B-b, 15B-b, 17C-b, D-b). The MLDs also showed distinct relationships with the residuals (Figs. 15B-c; 16B-c). We included Chl and MLD in the equations in the form logarithm ($c1 * X + c2 * \log X$) following Chierich et al. (2012). The following sections explain the classification of subzones in the oceans. The subzones are defined in Table 4, and the derived regression coefficients are listed in Tables 6 and 7.

Pacific ocean

The Pacific Ocean was divided into four zones for purposes of TA estimation as described in Sect. A1. We further divided it into 16 time-varying subzones, with borders defined on the basis of the distributions of SST, SSS, and SSDH, partly in accord with the methods of Sugimoto et al. (2012) and Iida et al. (2015).

Western equatorial-subtropical subzones (TA zone 1WP)

TA zone 1WP (SSDH > 0.8 m) covered a wide range in the western to central Pacific. The nTA within 1WP was almost constant $\sim 2300 \mu\text{mol}\cdot\text{kg}^{-1}$. At subtropical latitudes in zone 1WP, the carbonate system closely follows a seasonal cycle (e.g., Chierici et al. 2006), whereas non-seasonal variability associated with ENSO characterizes the carbonate system near the equator (e.g., Feely et al. 2006). Based on this difference, zone 1WP was divided into four subzones: two north and south subtropical subzones (1WP-1NWP and 1WP-2SWP, respectively) and two equatorial subzones (1WP-3WEQ and 1WP-4CEQ). At the equator, high salinity, low temperature, and high DIC water is brought to the surface from below by upwelling. There is a salinity gradient along the equator from high salinity in the east to low salinity in the west (Ishii et al. 2009). This part of 1WP was therefore divided into two equatorial subzones, 1WP-3WEQ, the western warm pool with $\text{SSS} < 34.7$ and $\text{SST} > 27.5$, and 1WP-4CEQ, the equatorial divergence area. The boundaries between the subtropical and equatorial regions of 1WP were defined by SSDH minima as proxies for the North and South Equatorial Currents.

Whereas the subtropics were previously thought to be less productive because of a lack of nutrients, it has recently been pointed out that nitrogen fixation and dissolved organic nutrients are important sources of nitrogen for primary production in the ocean (e.g., Hashihama et al. 2013). In addition to biological processes, winter vertical mixing and seasonal expansion and contraction of the subtropical gyres affect nDIC seasonality (e.g., Ayers and Lozier 2012; Fassbender et al. 2017). Consequently, nDICs in summer and winter are different under the same SST and SSS conditions, especially at relatively high latitudes in the subtropics. We took this seasonality into account by formulating monthly equations for the subtropical North Pacific to avoid amplification of the standard errors of the MLR by seasonal effects. We used a similar procedure for the South Pacific, but we used seasonal rather than monthly equations because we had insufficient data for the latter.

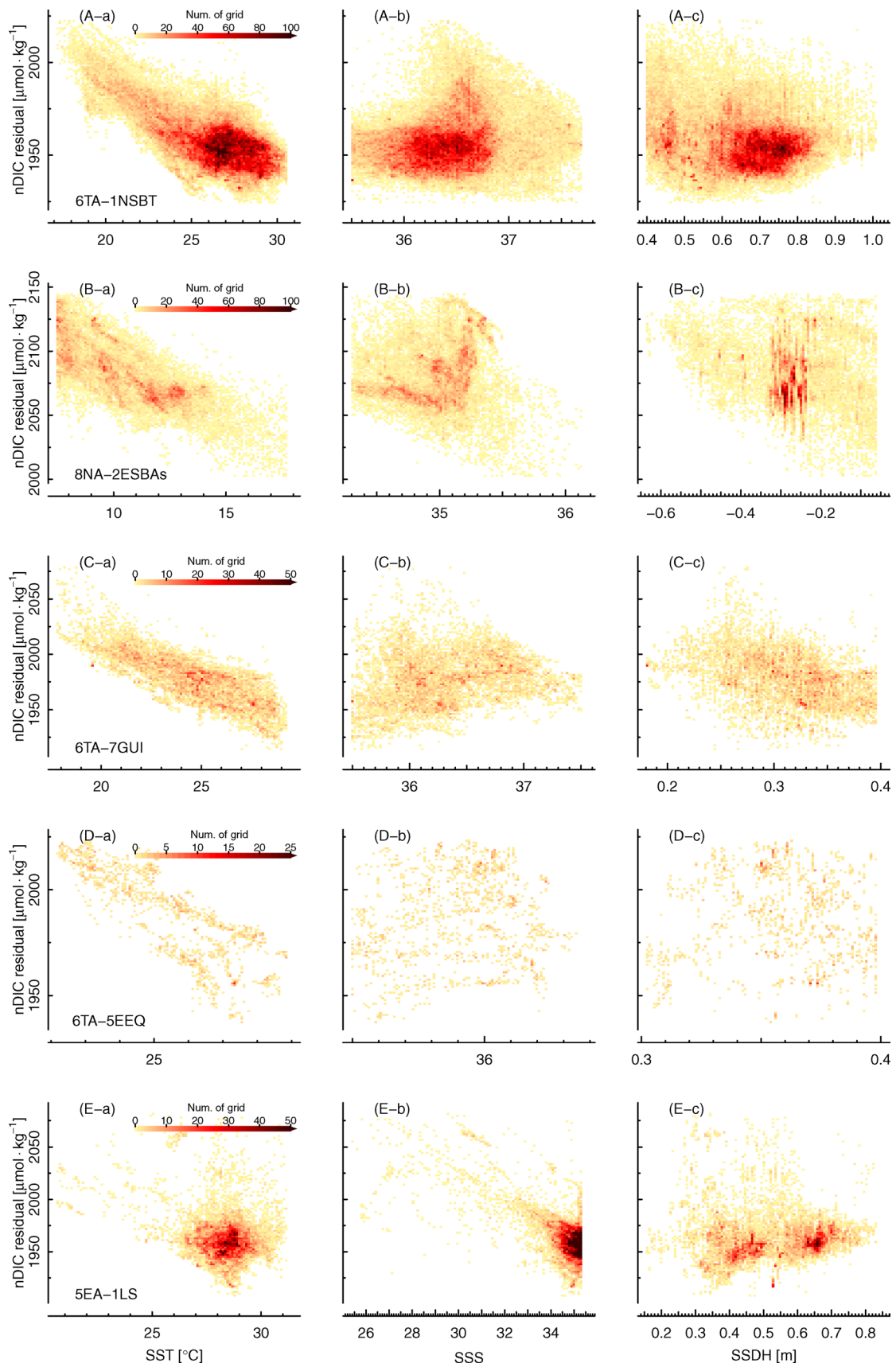


Fig. 11 The same as Fig. 10, but for the Atlantic Ocean

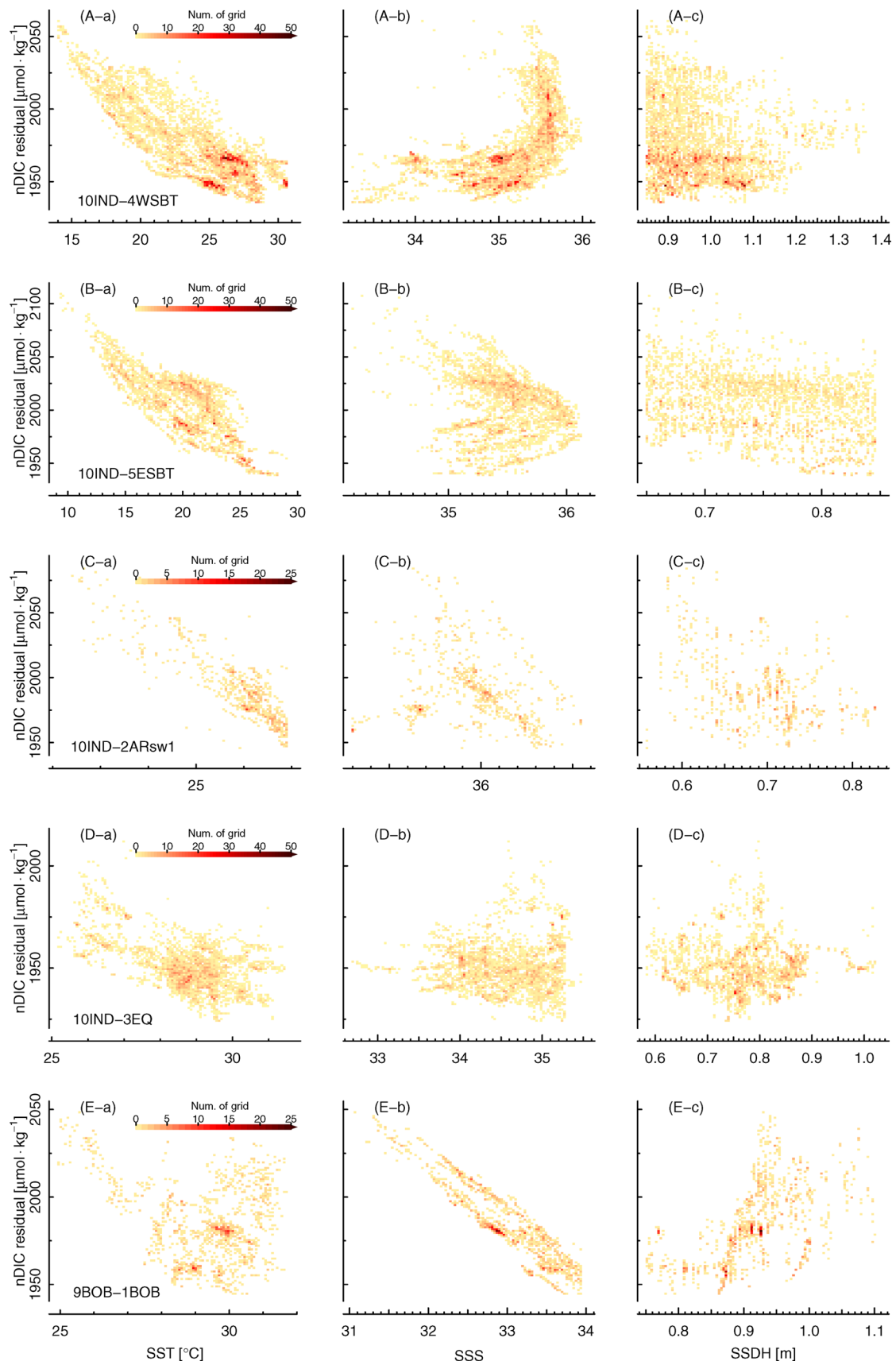


Fig. 12 The same as Fig. 10, but for the Indian Ocean

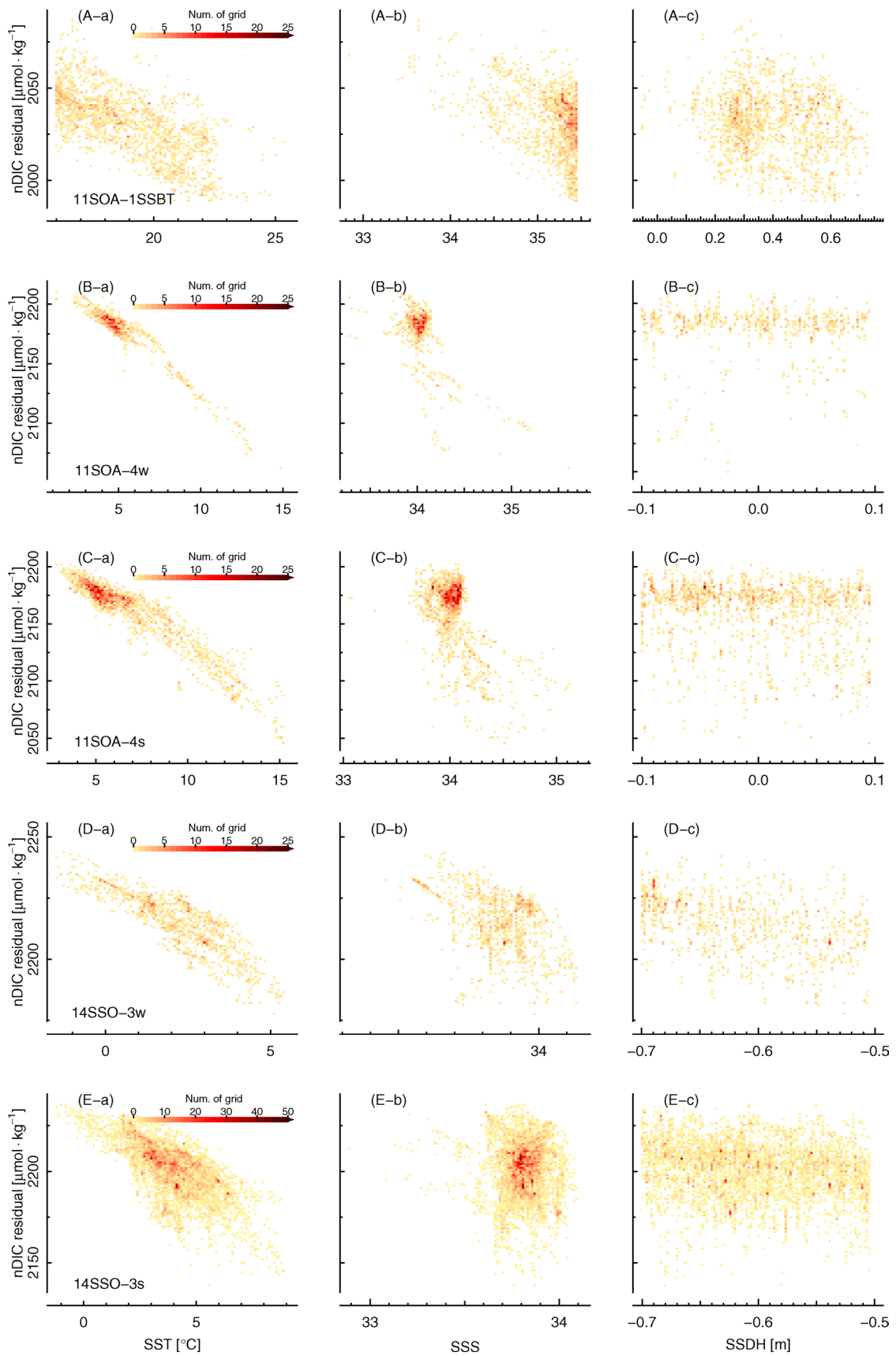


Fig. 13 The same as Fig. 10, but for the Southern Ocean

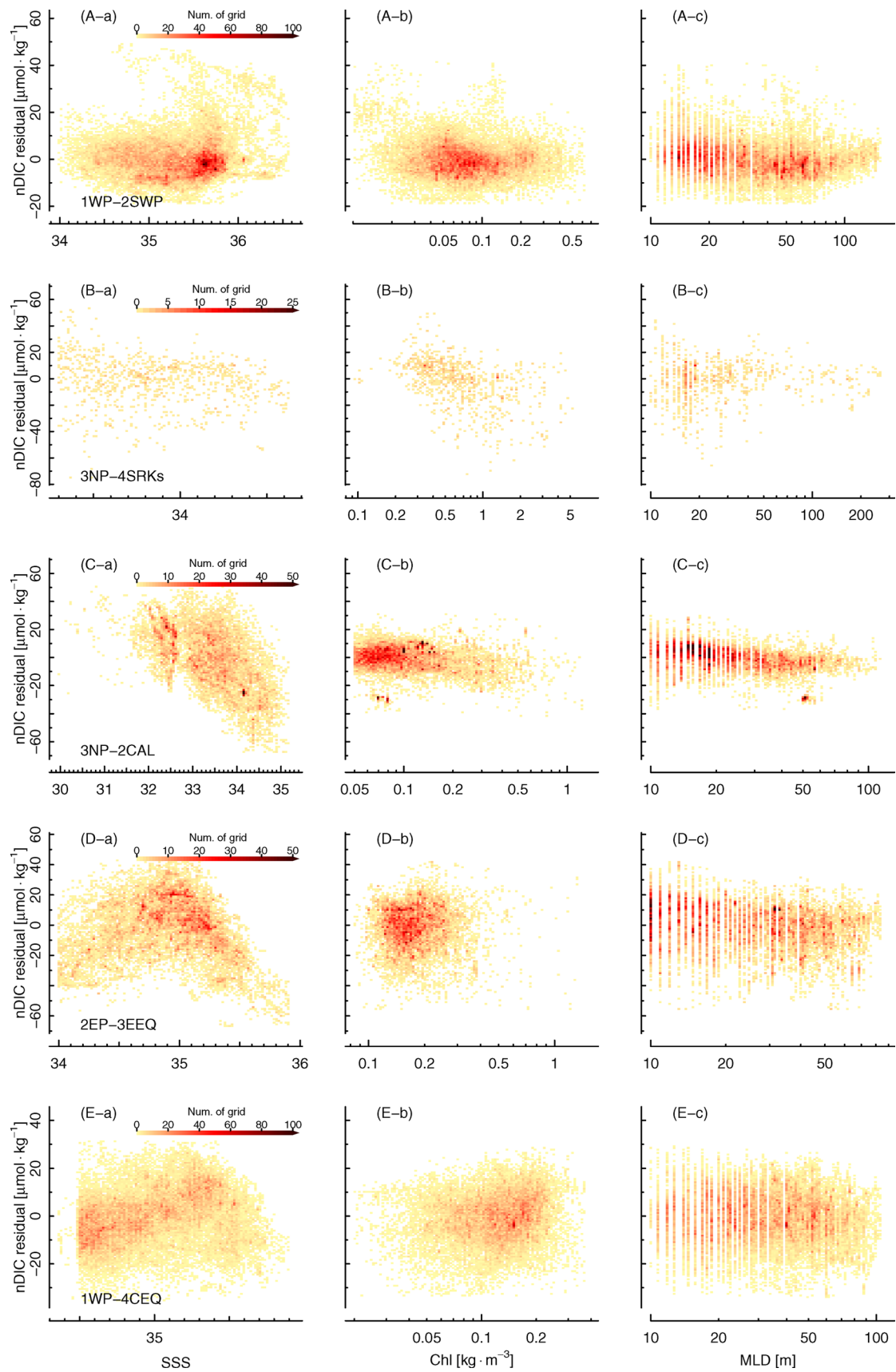


Fig. 14 Relationships of nDIC residuals versus SSS (left), Chl (center), and MLD (right) in representative subzones of the Pacific Ocean. Coloring indicates number of data in each grid. Residuals for SSS were calculated via MLR using SST alone as the explanatory variable; those for Chl via MLR using SST, SSS, and SSDH as explanatory variables; and those for MLD via MLR using SST, SSS, SSDH, and Chl as explanatory variables. The x -axes for Chl and MLD are logarithmic. Abbreviations of subzone names are defined in the text

Eastern equatorial subzones (TA zone 2EP)

TA zone 2EP, the area with SSDHs of 0.2–0.8 m, was divided into northern and southern parts by the SSDH maximum to the northern rim of the equatorial upwelling zone, and we further divided the two parts into two and three subzones, respectively. The southern three subzones were (1) the central-to-eastern equatorial divergence zone (2EP-3EEQ) defined as $SSS > 34$ and characterized by high DIC, high salinity, and low temperature (e.g., Feely et al. 1999); (2) the coastal upwelling area off Peru, south of 15°S (2EP-1PERU), which has oceanographic characteristics similar to equatorial (Friederich et al. 2008); and (3) the permanently low-salinity ($SSS < 34$) area off Panama (2EP-2EPFP) referred to as the eastern Pacific fresh pool (Alory et al. 2012), where both the pCO_2 and salinity are low (Brown et al. 2015). The highest nDIC residuals after elimination of SST effects in the 2EP-3EEQ subzone were observed at an SSS of about 34.9 (Fig. 14D-a), which corresponds to a subsurface salinity maximum. The northern two subzones were off Costa Rica (2EP-4COS) to the area east of 105° W and the SSDH less than 0.7 m, which shows the typically high pCO_2 related to high wind speed (Brown et al. 2015), and the remainder of the 2EP zone, the northeastern equatorial subzone (2EP-5NEEQ).

Subpolar subzones (TA zones 3NP and 4WSAG)

TA zone 4WSAG, the western subarctic gyre, is characterized by a SSDH less than 0.2 m. The nDIC in the gyre are homogeneous relative to the transition area as the case of nTA, and it was not divided into any subzones during the winter (4WSAG-1w). During the summer, however, it was divided into two subzones (4WSAG-2LTs and 4WSAG-3HTs) at an SST of 7.5 °C, which corresponds to a slight inflection point of the nDIC-SST relationship.

TA zone 3NP, the subtropical-subpolar transition zone, is characterized by steep gradients of SSS and TA as well as SSDH. Seawater in this zone can be considered to be hypothetical mixtures of subtropical and subarctic seawaters (Kakehi et al. 2017). We first defined the southern area of the 3NP zone as a nutrient-depleted, subtropical-like area with $SST > 16$ °C, and the northern area as a low-SST region around the western subarctic gyre (3NP-6NSBA) with a

$SST < 5$ °C. The subtropical-like area was divided into two subzones by the SSDH maximum along 120° W, an eastern boundary subzone off California (3NP-2CAL), which is affected by CO₂ rich subsurface seawater (Alin et al. 2012), and a northern subtropical Pacific subzone (3NP-1NSBT). The intermediate SST ($5 < SST < 16$ °C) area was divided primarily on the basis of differences between nDIC–salinity relationships into three subzones, a southern subzone with $SSDH > 0.35$ m (3NP-3STR), a subzone off Sanriku with $SSDH < 0.35$ m and $SSS > 33.3$ (3NP-4SRK), and an eastern subzone with $SSDH > 0.35$ m and $SSS < 33.3$ (3NP-5ESBA). Overall, in the transition-subarctic subzones, the nDIC residuals after elimination of SST variability were strongly correlated with SSS (Fig. 14C-a), and the nDIC residuals after elimination of SST/SSS/SSDH variability were correlated with Chl concentrations (Fig. 14B-b). Because Chl data are unavailable during winter in high latitudes, these subzones were treated separately during the winter (November–February) and summer (March–October) seasons.

Atlantic Ocean

Equatorial and subtropical subzones (TA zones 5EA 6TA)

In the equatorial Atlantic, large rivers such as the Congo and Amazon have a large effect on both the salinity and carbonate system (Lefevre et al. 2010; Ibáñez et al. 2015). TA zone 5EA, the area characterized by $SSS < 35.5$, was defined as a single subzone in the equatorial Atlantic (5EA-1LS). After elimination of SST variability, nDIC residuals in this subzone were strongly correlated with SSS (Fig. 15E-a). TA zone 6TA was divided into eight subzones in a manner similar to the division of Pacific. The western and eastern Atlantic were distinguished by $SSDH = 0.4$ m. The western Atlantic corresponded to TA zone 1WP and was divided into a subtropical North Atlantic (6TA-1NSBT), South Atlantic (6TA-2SSBT) and western equatorial (6TA-3WEQ) subzones on the basis of SSDH minima in a manner similar to the division of subzones in TA zone 1WP. To disentangle the complexity of the Atlantic eastern boundary systems, we divided the eastern Atlantic into six subzones based on SSDH maxima. Coastal upwelling controls the surface CO₂ in the Benguela Current system (Santana-Casiano et al. 2009) and the Guinea dome (Lefevre et al. 1998), and seasonal upwelling lowers SST and increases surface DIC in the eastern equatorial Atlantic (Parard et al. 2010). We distinguished the Angola-Benguela subzone (6TA-4ABR) based on the southeastern Atlantic SSDH maximum along 8° S. The subzone off Guinea (6TA-7GUI) was distinguished on the basis of the SSDH maximum around 15–20° N. The eastern equatorial upwelling subzone (6TA-5EEQ) was located between subzones 6TA-4ABR and 6TA-7GUI. The remainder of the northern area of TA zone 6TA was divided into

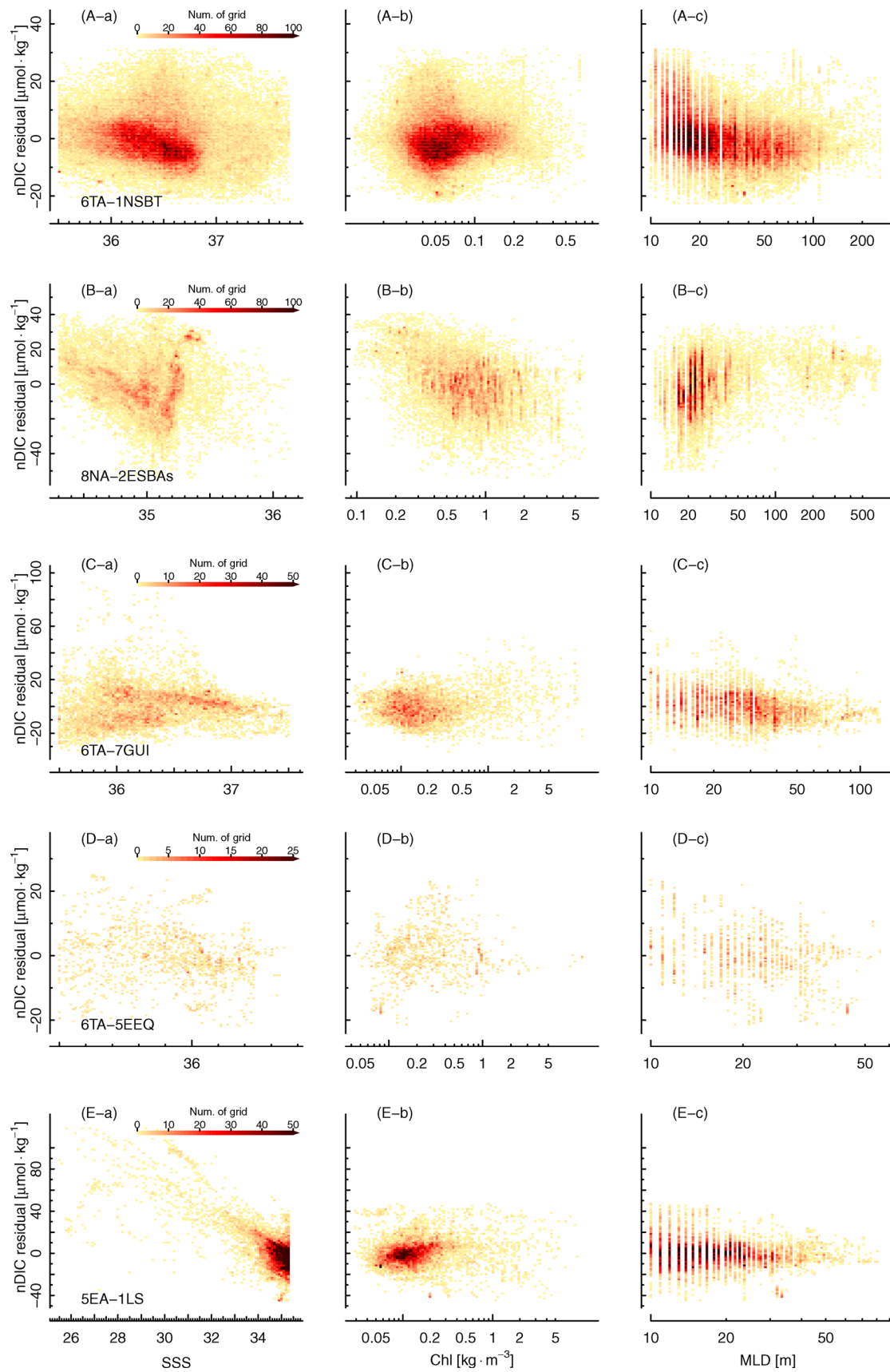


Fig. 15 The same as Fig. 14, but for the Atlantic Ocean

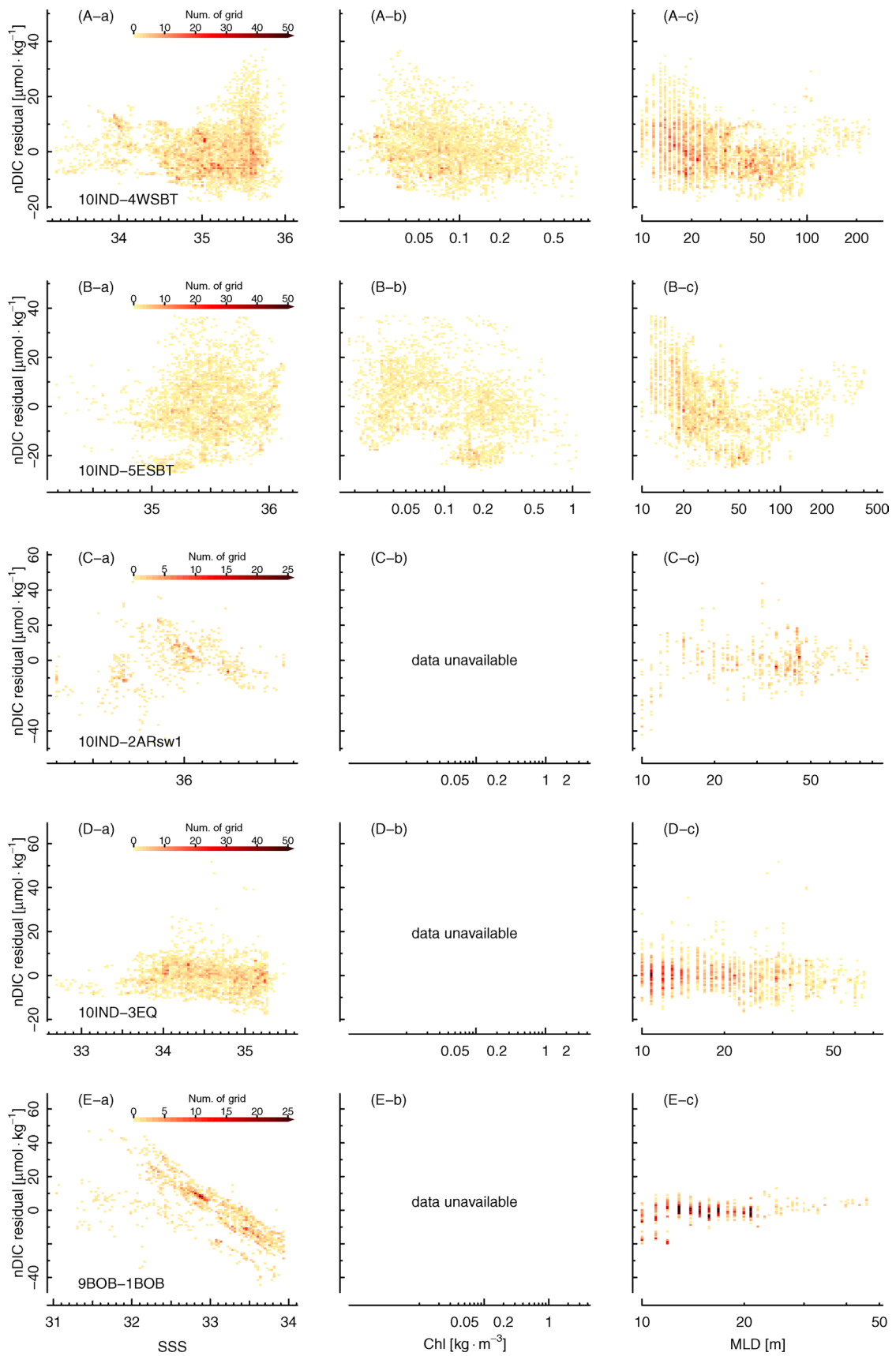


Fig. 16 The same as Fig. 14, but for the Indian Ocean

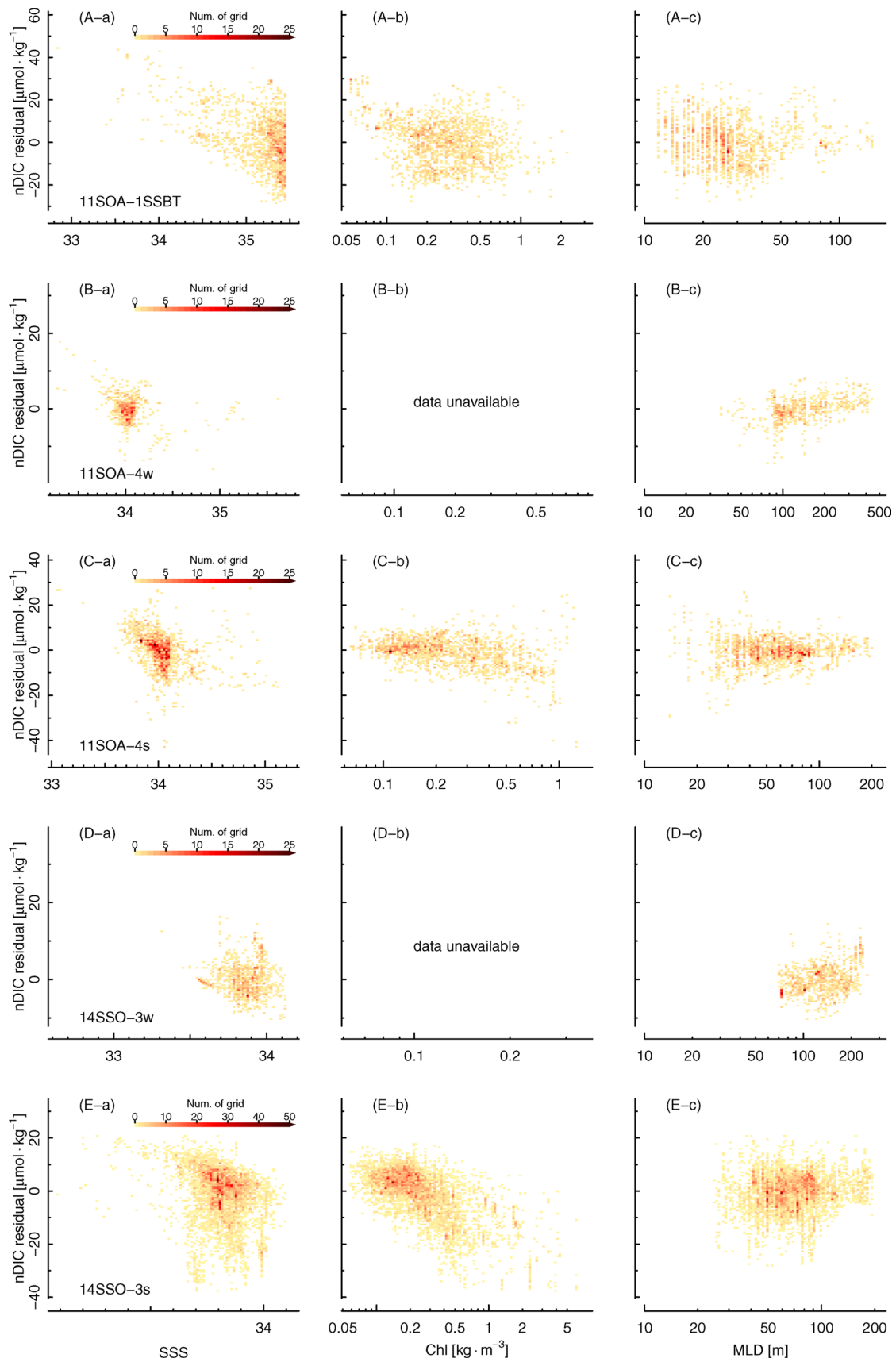


Fig. 17 The same as Fig. 14, but for the Southern Ocean

Table 6 Regression coefficients for estimating nDIC. Abbreviations of subzones are defined in the text

TAzone	biome	a	b	c1	c2	c3	d1	d2	d3	e1	e2	f1	f2	f3	g1	g2	msst	msss	mssh	σ	N	
IWP	INWP	-	-	-	-	-	-	-	-	-	-	-	-	-	-	-	-	-	-	-	-	
	2SWP	*1	-	-	-	-	-	-	-	-	-	-	-	-	-	-	-	-	-	-	-	
	3WEQ	1951.1	0.94	-4.04	1.613	-	-0.04 ²	4.37	-	-26.7	-61.8	-	-	-	-	-	29.50	34.07	1.033	5.2	31724	
	4CEQ	1972.2	1.04	-11.81	0.975	-	12.82	-29.59	-	-40.8	-120.7	-	-	-	-	-	28.74	35.01	1.015	9.8	32440	
	2EP	1PERU	2039.6	1.27	-4.69	0.082	-	-17.68	-23.67	-	-87.9	406.7	-	-	-	-	-	19.62	35.28	0.598	4.7	3631
		2EPPP	1987.5	1.53	-3.96	0.447	-	3.85	5.65	-	-132.2	-154.7	-	-	-	-	-	26.85	33.48	0.677	7.2	2379
		3EEQ	2041.2	0.91	-8.97	-0.210	-	-8.34	-57.70	-	-113.3	137.7	-	-	-	-	-	24.85	34.93	0.656	13.8	16016
		4COS	1994.6	1.32	-12.43	1.066	-	4.77	2.86	-	-127.1	100.3 ²	-	-	-	-	-	27.86	33.44	0.633	12.3	5121
		5NEEQ	1977.5	1.06	-4.48	0.200	-	2.10	1.87	-	-85.9	-23.7 ²	-	-	-	-	-	27.20	33.93	0.727	7.2	13645
	3NP	INSBT	2056.4	1.26	-6.68	-0.071	-	-36.91	-0.07 ²	-	-18.7	-59.4	0.53 ²	-	2.65	0.355	-15.77	20.65	34.05	0.563	8.9	18461
2CAL		2120.3	0.91	-4.83	-0.104	-	-30.63	-4.45	-	-38.4	-150.3	-22.11	-2.97	0.126	-	-14.04	19.42	33.43	0.656	6.1	11663	
3STR		2121.2	0.89	-8.99	0.119	-	-30.41	1.18	-	-16.8	1.94 ²	-	-	-	-	-	11.67	33.32	0.517	5.8	7851	
sum		2108.4	0.93	-7.85	0.081	-	-26.55	-2.54	-	-49.6	-56.1	-4.36	-9.47	-	-	-	12.83	33.25	0.528	7.9	13582	
4SRK		2126.7	0.88	-11.19	-0.021 ²	-	-17.07	7.31	-	-20.6	392.7	-	-	-	-	-	10.35	33.76	0.301	4.6	884	
5ESBA	sum	2100.1	1.37	-10.39	0.293	-	-13.52	6.86	-	-46.6	59.6 ²	2.25	-15.33	-	-	-	11.10	33.86	0.295	11.7	981	
	win	2186.8	0.80	-9.65	-0.186	-	-36.01	5.82	-	-37.9	216.1	-	-	-	-	-	7.11	32.74	0.288	5.5	1803	
	sum	2159.8	0.92	-7.59	-0.039 ²	-	-28.77	-38.10	-	-55.8	-235.4	-10.24	-11.65	-	-	-	10.17	32.70	0.276	10.4	4351	
	win	2226.8	0.81	-11.13	-1.136	-	-27.27	3.21 ²	-	-42.0	102.3	-	-	-	-	-	3.40	32.90	0.263	7.7	1288	
	sum	2207.7	0.79	-13.18	-1.609	-	-22.34	16.73	-	-12.9 ²	-3.2 ²	-4.78	-18.28	-	-	-	3.39	32.95	0.289	10.8	1017	
4WSAG	1	2233.7	0.78	-8.38	-0.675	-	11.00	16.82	-	6.5	-116.7	-	-	-	-	-	3.97	32.88	0.129	8.4	3166	
	sum1	2230.9	0.93	-8.64	-0.610	-	8.75	-16.01	-	-14.3	-168.8	-9.55	-5.42	-	-	-	4.36	32.98	0.132	9.1	2215	
	sum2	2147.2	0.88	-9.33	-0.031 ²	-	2.11	-15.25	-	-6.1 ²	711.0	3.81	-15.62	-	-	-	11.40	32.73	0.133	13.6	3540	
	win	2233.7	0.78	-8.38	-0.675	-	11.00	16.82	-	6.5	-116.7	-	-	-	-	-	3.97	32.88	0.129	8.4	3166	
	sum	2230.9	0.93	-8.64	-0.610	-	8.75	-16.01	-	-14.3	-168.8	-9.55	-5.42	-	-	-	4.36	32.98	0.132	9.1	2215	
5EA	ILS	1955.9	0.89	-3.58	0.814	-	-14.75	-0.47	-	26.7	106.5	-	-	-	-	-	28.37	34.67	0.532	9.1	12203	
	INSBT	*1	-	-	-	-	-	-	-	-	-	-	-	-	-	-	-	-	-	-	-	
	2SSBT	*1	-	-	-	-	-	-	-	-	-	-	-	-	-	-	-	-	-	-	-	
	3WEQ	1963.2	0.73	-6.10	1.532	-	5.53	-22.80	-	7.6	-292.2	-	-	-	-	-	27.42	36.04	0.482	6.8	7506	
	4ABR	2000.0	0.92	-4.56	0.116	-0.028	-20.55	-26.94	43.24	-46.2	-109.7	-	-	-	-	-	22.34	36.08	0.320	8.3	2943	
	5EEQ	1987.4	1.19	-7.99	0.091 ²	-	-5.32	-20.06	-	-66.4	-1698	-	-	-	-	-	25.54	35.92	0.361	6.0	1500	
	6GST	1969.1	0.85	-4.42	0.089	-	-6.51	13.46	-	-3.0	-123.6	-	-	-	-0.011 ²	-4.56	27.22	36.12	0.293	5.3	4502	
	7GUI	2036.8	1.18	-7.20	-0.408	-0.071	2.67	-3.55	-3.93	-47.9	-188.0	-	-	-	0.202	-19.67	24.57	36.34	0.314	8.0	9452	
	8NESBT	2029.9	1.17	-4.15	-0.059	-	-1.35	-2.29	-	-51.3	-43.9	-	-	-	0.152	-11.19	21.19	36.40	0.225	6.1	14773	
	9NSBT	2008.2	1.25	-8.40	0.733	-	-2.85	-15.43	-	-36.6	70.5	-3.53	-5.09	-	-0.402	5.18	15.47	35.87	0.133	6.2	11106	
	ISSBA	2053.0	0.97	-5.08	0.091	-	-32.22	1.07	-	23.9	-40.3	-	-	-	0.402	-15.20	23.16	34.67	-0.086	8.9	8613	
	2SESBA	2087.4	0.72	-10.36	-0.141	-	-23.41	0.00	-	9.3	-96.4	-	-	-	0.032	-3.55	13.31	35.35	0.030	6.2	1532	
	sum	2035.7	0.67	-7.20	-0.279	-	-29.09	0.00	-	-10.2	-47.2	-0.74 ²	-5.99	-	0.008	6.48	13.92	35.21	0.018	9.7	5084	
	8NA	1GLB	2109.6	0.78	-6.00	-0.160	-	-34.88	-0.55	-	36.2	89.6	-	-	-	-0.071	20.85	6.54	32.97	-0.259	9.5	1059
		sum	2060.7	0.78	-2.71	-0.234	-	-39.66	1.39	-	37.5	102.2	-1.46	-3.12	-	-0.089	28.92	8.39	33.05	-0.246	16.2	6826
win		2059.3	1.21	-7.75	-0.130	-	-15.99	6.16	-	-8.2	75.0	-	-	-	-0.022	11.91	8.69	35.11	-0.264	3.9	9279	
sum		2012.3	1.21	-7.39	0.129	-	-22.72	10.31	-	-2.1 ²	104.8	0.05 ²	-3.65	-	-0.042	17.99	10.76	34.99	-0.267	9.1	21433	
win		2058.3	1.27	-4.35	0.116	-	-28.74	-4.01	-	-6.8	138.4	-	-	-	-0.043	15.78	6.38	35.03	-0.315	2.2	7856	
sum	2001.6	1.27	-5.43	0.124	-	-20.96	14.12 ²	-	-23.5	41.2	0.62	-5.30	-	-0.125	29.13	6.18	34.99	-0.350	10.4	9542		

Table 6 (continued)

TAzone	biome	a	b	c1	c2	c3	d1	d2	d3	e1	e2	f1	f2	f3	g1	g2	msst	mss	mssh	σ	N
9BOB	IBOB	1986.1	1.22	-2.83	0.050	-	-33.37	0.70	-	-31.2	24.1	-	-	-	-	-	29.42	33.04	0.918	3.8	1608
10IND	IAREX	1946.9	1.22	-3.29	1.125	-	-5.06	-9.33	-	-32.1	58.7 ²	-	-	-	-	-	29.25	36.10	0.714	6.1	1528
	2AR	nsw	1965.3	1.22	-11.09	0.241 ²	-9.70	4.84	-	39.8	135.2 ²	-	-	-	-	-	26.52	36.15	0.693	8.5	1676
		sw1	2007.4	1.22	-25.77	-1.476	-6.19	-56.06	-	-53.4	-364.1	-	-	-	-	-	25.94	35.97	0.699	8.0	822
		sw2	1956.2	1.22	-8.35	5.420	-14.34	-7.87	-	-27.9	505.9	-	-	-	-	-	27.72	36.21	0.722	2.9	738
	3EQ	1958.5	1.22	-5.72	0.253	-	-3.34	-3.19	-	-18.8	-49.9	-	-	-	-	-	28.77	34.55	0.778	5.1	3935
	4WSBT	*	-	-	-	-	-	-	-	-	-	-	-	-	-	-	-	-	-	-	-
	5ESBT	2065.4	1.51	-7.22	0.297	-	10.27	0.17 ²	-	11.5	-363.8	-	-	-	0.191	-21.47	20.34	35.50	0.751	10.7	4170
TAzone	biome	a	b	c1	c2	c3	d1	d2	d3	e1	e2	f1	f2	f3	g1	g2	msst	mss	mssh	σ	N
11SOA	ISSBT	2037.6	0.69	-6.76	0.230	-	-25.39	-3.03	-	-20.7	-89.8	12.19	-13.78	-	0.241	-11.61	18.95	35.21	0.398	9.1	1925
	2	win	2077.7	0.89	-9.41	0.025	-22.33	0.25	-	-13.9	50.2	-	-	-	-	-	13.34	34.88	0.442	2.1	824
		sum	2081.8	0.93	-8.65	-0.140	-29.66	1.81	-	-21.5	21.5 ²	-6.62	-8.87	-	-	-	13.13	34.56	0.409	6.2	632
	3	win	2152.3	0.51	-9.98	-0.207	-19.17	4.28	-	19.3	-81.3	-	-	-	-	-	7.78	34.13	0.189	2.9	743
		sum	2112.9	0.85	-9.50	-0.311	-24.41	-1.38	-	6.3	90.5	-2.26	-5.09	-	-	-	10.75	34.32	0.190	5.9	2002
	4	win	2175.8	0.72	-8.51	-0.429	-12.59	8.50	-	-5.7	-54.6	-	-	-	-	-	5.37	34.05	0.000	2.4	860
		sum	2166.2	0.77	-8.27	-0.162	-23.77	5.20	-	-6.6	16.6 ²	-20.59	0.50 ²	-	-	-	6.84	34.04	-0.003	3.7	2039
12SOI	ISSBT	1968.5	1.29	-6.21	-0.079	-	-41.56	-6.53	-	-23.9	-51.5	1.00 ²	-10.56	-	-0.249	12.28	18.44	35.49	0.551	6.9	1896
	2	win	2099.4	0.83	-11.50	-0.138	-14.23	-11.44	-	-12.0	-291.1	-	-	-	-	-	11.41	34.96	0.566	2.3	1318
		sum	2096.3	0.70	-9.03	0.416	-26.71	-7.17	-	-16.1	14.1 ²	-24.82	0.16 ²	-	-	-	12.30	34.74	0.560	4.1	3309
	3	win	2116.1	0.89	-9.66	-0.259	-21.19	-1.42 ²	-	1.7 ²	-20.1 ²	-	-	-	-	-	10.16	34.75	0.444	2.4	380
		sum	2096.5	0.74	-9.94	-0.232	-26.45	-2.51	-	-21.1	26.4 ²	-7.45	-3.48	-	-	-	12.00	34.58	0.429	4.8	1411
	4	win	2120.9	0.86	-11.29	-0.392	-16.05	7.36	-	-11.8	-26.9 ²	-	-	-	-	-	10.13	34.48	0.186	2.5	194
		sum	2130.8	0.86	-9.11	-0.309	-29.66	8.19	-	-16.1	-6.7 ²	-22.51	-1.92	-	-	-	10.27	34.21	0.199	4.5	1073
	5	win	2161.9	0.89	-8.52	-0.365	-19.09	3.85	-	-11.0	31.1 ²	-	-	-	-	-	7.22	34.01	-0.010	2.2	290
		sum	2154.2	0.89	-8.23	-0.398	-29.38	2.00 ²	-	-17.3	-57.4 ²	-16.79	-1.68	-	-	-	8.45	34.02	-0.002	3.5	1223
13SOP	ISSBT	2024.0	1.34	-5.39	0.138	-0.082	-29.28	8.11	3.88	-24.9	-190.4	-0.73 ²	-4.94	-	0.129	-5.86	18.45	35.39	0.691	6.3	11945
	2	win	2068.5	1.02	-10.58	-0.113	-20.60	1.47	-	0.8 ²	-91.8	-	-	-	-	-	13.68	35.02	0.626	3.5	3684
		sum	2058.9	0.59	-9.84	0.248	-19.20	8.80	-	-12.1	31.6 ²	-4.65	-6.87	-	-	-	13.69	34.86	0.589	6.0	3324
	3	win	2136.2	0.83	-10.01	0.191	-15.82	2.02	-	-15.5	-311.9	-	-	-	-	-	8.41	34.38	0.426	2.9	1654
		sum	2113.3	0.68	-8.42	0.041	-25.09	2.41	-	-23.6	-79.3	-1.75 ²	-7.22	-	-	-	9.75	34.28	0.406	4.1	4000
	4	win	2153.4	0.94	-10.48	-0.522	-3.77	27.61	-	-8.6	226.0	-	-	-	-	-	6.95	34.21	0.215	2.2	535
		sum	2140.1	0.66	-8.42	0.029	-25.39	-0.30 ²	-	4.7	178.5	-9.77	-3.17	-	-	-	8.18	34.15	0.223	3.3	2040
	5	win	2163.4	0.99	-10.33	-0.405	1.10 ²	32.17	-	-12.8	73.9	-	-	-	-	-	6.34	34.18	0.021	1.7	294
		sum	2149.9	0.75	-7.48	0.253	-30.45	-3.13	-	-20.1	-105.6	-6.15	-2.51	-	-	-	7.62	34.10	0.001	3.4	944
14SSO	1	win	2184.1	0.78	-8.45	-0.356	-17.00	1.41	-	-22.8	-29.9 ²	-	-	-	-	-	4.84	33.99	-0.194	2.8	1385
		sum	2165.2	0.81	-7.77	-0.273	-30.26	-0.50	-	-23.3	19.5 ²	-4.43	-4.23	-	-	-	6.36	33.96	-0.197	4.0	5603
	2	win	2198.5	0.82	-6.95	-0.434	-16.59	4.12	-	-24.8	3.8 ²	-	-	-	-	-	3.74	33.90	-0.399	2.1	1250
		sum	2181.8	0.73	-7.40	-0.133	-29.89	0.97 ²	-	-16.6	-10.2 ²	-12.96	-3.91	-	-	-	5.57	33.83	-0.397	4.4	5396

Table 6 (continued)

TAzone	biome	a	b	c1	c2	c3	d1	d2	d3	e1	e2	f1	f2	f3	g1	g2	msst	msss	mssh	σ	N
3	win	2215.0	0.58	-6.23	-0.583	-	-3.83	15.16	-	-30.9	128.8	-	-	-	-	-	2.21	33.87	-0.617	3.6	1253
	sum	2187.3	0.73	-7.64	-0.317	-	-24.76	-11.75	-	6.5	-55.5	-0.44	-8.41	-	-	-	4.01	33.82	-0.603	5.9	6397
4	win	2225.4	0.72	-6.48	-0.190	-	5.69	57.69	-	-17.2	125.9	-	-	-	-	-	0.88	33.82	-0.792	2.9	2238
	sum	2207.0	0.73	-7.08	-0.597	-	-13.11	7.15	-	-20.5	-95.3	-12.20	-5.64	-	-	-	2.92	33.79	-0.815	4.8	6714
5	win	2236.5	0.71	-6.65	0.146	-	-6.15	25.22	-	-36.1	39.9	-	-	-	-	-	0.05	33.79	-0.993	3.3	2111
	sum	2207.4	0.79	-6.54	-0.765	-	-6.30	13.54	-	0.8 ^{#2}	-86.3	2.44	-9.94	-	-	-	1.67	33.77	-1.001	7.6	10338
6	win	2245.4	0.68	-6.81	-0.356	-	12.47	8.79	-	7.4	-15.4	-	-	-	-	-	-0.38	33.95	-1.218	2.5	1724
	sum	2219.3	0.33	-6.21	0.761	-	-13.22	2.77	-	-9.5	-54.5	-8.90	-11.39	-	-	-	0.60	33.82	-1.219	8.6	13487

The regression equation is $nDIC = a + b \text{ (year - 2005)} + c_1 \text{ mSST} + c_2 \text{ mSST}^2 + c_3 \text{ mSST}^3 + d_1 \text{ mSSS} + d_2 \text{ mSSS}^2 + d_3 \text{ mSSS}^3 + e_1 \text{ mSSDH} + e_2 \text{ mSSDH}^2 + f_1 \text{ Chl} + f_2 \log(\text{Chl}) + f_3 (1/\text{Chl}) + g_1 \text{ MLD} + g_2 \log(\text{MLD})$. In this equation, mSST is SST - msst, where msst is the representative SST in each zone. The variables mSSS and mSSDH are defined in a similar manner

^{#1}Monthly/Seasonal coefficients are shown in Table 7

^{#2}Coefficients are considered insignificant if the type I error rate exceeds 10%

three subzones, a Gulf Stream subzone (6TA-6GST) west of 60° W; a northeastern subtropical subzone (6TA-8NESBT) defined by SST > 18 °C, a temperature that corresponds to a threshold for nutrient depletion; and a northern subtropics subzone (6TA-9NSBT) defined by SST < 18 °C.

Subarctic subzones (TA zones 7NEA and 8NA)

In the northern North Atlantic, subtropical seawaters are brought to high latitudes by the North Atlantic Current, and seawater characterized by high SST and high SSS is widely distributed in this area (e.g., Rossby 1996). However, low SST and low SSS areas that are influenced by Arctic seawater are distributed around Greenland, the Labrador Sea, and off Newfoundland (e.g., Mertens et al. 2014). These differences of SST and SSS accentuate the contrast of carbonate biogeochemistry between the eastern and western parts of the northern North Atlantic (e.g., Körtzinger et al. 2008; Schuster et al. 2009). The lowering of SST due to deep convection in winter results in a positive correlation between MLD and DIC (e.g., Olsen et al. 2008).

Nutrient-depleted conditions were associated with SST > 18 °C in the subtropics-like subzone (7NEA-1SSBA). These conditions (SST > 18 °C) were found in both TA zones 7NEA and 8NA. The remainder of TA zone 7NEA was defined as a single subzone (7NEA-2SESBA). The remainder of TA zone 8NA was divided into a western subzone with SSS < 34.3 (8NA-1GLB), which mainly included areas around Greenland, the Labrador Sea, and off Newfoundland, and a North Atlantic Current area with SSS > 34.3. The latter was further divided into a southern subzone (8NA-2ESBA) and a northern subzone (8NA-3NSBA) by SSTs greater than or less than 7.5 °C, respectively. Those subzones were distinguished between winter (Nov.–Feb.) and summer (Mar.–Oct.) based on the availability of Chl data. The fact that residuals of nDIC after elimination of effects due to SST, SSS and SSDH were well correlated with MLD as well as Chl (Fig. 15B-c, B-b) indicated that MLD reduced the uncertainty of TA in these subzones.

Indian Ocean

In the northern Indian Ocean, the monsoons influence the carbonate system in the Arabian Sea, and the Ganges–Brahmaputra River controls the oceanographic system in the Bay of Bengal (e.g., Sabine et al. 2000; Sarma 2003; Bates et al. 2006). The northern Indian Ocean is thought to be a small source of atmospheric CO₂, whereas the southern Indian Ocean is a strong sink and absorbs CO₂ during the austral winter (Sarma et al. 2013). TA zone 9BOB, the Bay of Bengal, was defined as a single subzone (9BOB-1BOB) in which nDIC was strongly controlled by SSS variability (Fig. 16E-a). In the Arabian Sea and off Somalia, the southwestern

Table 7 Regression coefficients for estimating nDIC in the subtropical Pacific, Atlantic and Indian Oceans. Abbreviations of subzones are written in the text

TAzone	biome		<i>a</i>	<i>b</i>	<i>c</i> ₁	<i>c</i> ₂	<i>c</i> ₃	<i>d</i> ₁	<i>e</i> ₁	<i>msst</i>	<i>msss</i>	<i>mssh</i>	σ	<i>N</i>
1IWP	1NWP	Jan	1974.3	1.15	-6.26	0.156	-0.004	-6.59	-18.8	23.47	34.73	1.252	3.8	16230
		Feb	1974.1	1.15	-6.17	0.191	0.000	-7.20	-18.3	23.56	34.70	1.215	4.0	14651
		Mar	1987.7	1.15	-6.83	0.114	0.002	-7.90	-21.6	21.89	34.68	1.198	4.2	11514
		Apr	1985.2	1.15	-5.40	0.161	-0.015	-4.02	-17.4	22.08	34.72	1.277	4.3	9252
		May	1982.3	1.15	-4.72	0.020	-0.022	-2.71	-13.8	23.55	34.67	1.204	5.6	10581
		Jun	1974.5	1.15	-5.59	0.096	0.015	1.41	-8.9	25.86	34.62	1.221	8.8	11965
		Jul	1965.8	1.15	-7.24	-0.081	-0.017	1.70	6.2	28.21	34.49	1.247	9.1	12527
		Aug	1967.0	1.15	-9.72	0.047	0.015	-3.39	6.6	28.18	34.52	1.182	8.0	11645
		Sep	1966.3	1.15	-7.53	-0.268	-0.078	-2.38	-3.2	27.98	34.63	1.190	7.8	10843
		Oct	1967.0	1.15	-5.62	-0.009	-0.087	-1.90	-7.6	26.90	34.59	1.179	6.5	10906
		Nov	1969.0	1.15	-5.80	-0.090	-0.013	-4.67	-15.2	25.70	34.63	1.221	4.4	13546
		Dec	1973.6	1.15	-5.87	-0.034	-0.008	-8.42	-17.5	24.28	34.73	1.204	3.7	11438
	2SWP	Win	1953.3	1.15	-6.05	0.384	0.062	-0.04	-48.6	27.32	35.29	1.056	6.3	5398
		Spr	1952.2	1.15	-4.86	0.128	0.005	-3.24	-50.5	26.14	35.28	1.077	4.7	11129
		Sum	1970.6	1.15	-6.41	0.311	0.014	-3.57	-28.8	22.86	35.41	1.040	4.1	7152
		Aut	1964.7	1.15	-4.92	0.072	0.003	-2.53	-44.7	24.91	35.39	1.038	5.1	7177
6TA	1NSBT	Jan	1947.7	0.98	-4.06	1.213	0.091	-3.87	-7.0	25.13	36.46	0.656	4.9	4797
		Feb	1949.5	0.98	-4.68	1.238	0.115	-1.37	-0.7	24.52	36.45	0.665	4.5	6707
		Mar	1952.2	0.98	-4.11	1.018	0.058	-2.47	-14.9	24.58	36.45	0.646	5.1	6961
		Apr	1953.9	0.98	-5.15	0.668	0.068	-8.09	-11.3	24.74	36.47	0.666	5.2	7784
		May	1956.3	0.98	-5.90	0.545	0.087	-4.31	-14.7	25.00	36.52	0.652	5.1	7270
		Jun	1951.9	0.98	-5.65	0.620	0.100	-5.05	-2.6	26.82	36.43	0.665	5.1	6766
		Jul	1952.0	0.98	-6.27	0.338	0.086	-3.91	-8.7	27.90	36.39	0.675	6.5	7251
		Aug	1947.0	0.98	-5.65	0.875	0.131	-3.10	-5.2	28.21	36.49	0.665	5.8	7573
		Sep	1945.2	0.98	-5.22	0.351	0.110	-4.29	-17.0	28.48	36.43	0.663	4.4	5472
		Oct	1946.4	0.98	-5.12	0.257	0.034	-5.23	-12.6	27.39	36.51	0.650	5.8	5354
		Nov	1945.6	0.98	-4.45	0.862	0.080	-1.35	-13.1	26.46	36.49	0.650	5.2	5163
		Dec	1944.7	0.98	-4.53	0.967	0.082	-3.74	0.6	25.94	36.42	0.679	4.7	4762
	2SSBT	Win	1976.7	1.11	-6.35	-1.301	-0.102	-8.66	-12.6	25.45	36.55	0.596	7.7	1884
		Spr	1958.4	1.11	-3.54	-0.353	-0.064	-12.98	-15.9	25.79	36.71	0.616	5.4	1763
		Sum	1991.5	1.11	-6.06	-0.323	-0.029	-8.08	-48.4	21.47	36.47	0.568	1.7	1619
		Aut	1990.7	1.11	-5.92	-0.259	-0.018	-7.98	-25.3	21.55	36.41	0.597	6.0	4153
10IND	6WSBT	Win	1973.4	1.33	-6.08	0.378	0.071	7.07	-29.1	24.56	35.31	0.965	6.2	2887
		Spr	1960.3	1.33	-3.54	0.112	-0.035	-4.96	4.2	25.85	35.00	1.003	2.8	1556
		Sum	1984.4	1.33	-8.39	0.508	0.031	-9.49	-1.7	20.76	35.40	0.963	2.4	1080
		Aut	1972.7	1.33	-2.59	0.107	-0.026	3.11	-2.0	24.68	34.80	0.966	4.2	1783

The regression equation is $nDIC = a + b(\text{year} - 2005) + c_1 \text{mSST} + c_2 \text{mSST}^2 + c_3 \text{mSST}^3 + d_1 \text{mSSS} + d_2 \text{mSSS}^2 + d_3 \text{mSSS}^3 + e_1 \text{mSSDH} + e_2 \text{mSSDH}^2$. In this equation, mSST is $SST - \text{msst}$, where msst is the representative SST in each zone. The variables mSSS and mSSDH are defined in a similar manner

monsoon causes coastal upwelling and brings cold seawater to the surface. The upwelling results in surface waters characterized by low temperatures and an extremely high content of CO_2 (e.g., Körzinger et al. 1997). In winter, the northeastern monsoon induces convective mixing (Sarma 2003) that results in a high correlation between SST and nDIC.

The Arabian Sea was defined as the area with $\text{SSS} > 35.3$ in the northern Indian Ocean and was divided into four seasonal subzones. The area with $\text{SST} > 28.3$ °C

(10IND-1AREX) was thought not to be affected by upwelling and was defined as a single subzone throughout the year. The area with $\text{SST} < 28.3$ °C was thought to be affected by lower seawater and was divided into two seasons, a SW monsoon season (Jun.–Sep.) and the remainder of the year (10IND-2AR_{nsw}). A threshold SST of 27 °C was used to further divide the former into two regions, the northwestern Arabian Sea (10IND-2AR_{sw1}), which is greatly affected by upwelling, and the remainder of the subzone

(10IND-2ARsw2), which is only moderately affected by upwelling. We distinguished the equatorial subzone into a northern Indian Ocean area characterized by SSS < 35.3 or an equatorial area characterized by SSDH < 0.85 m (10IND-3EQ).

The rest of the southern Indian Ocean was divided into two subzones, a western subtropical subzone (10IND-4WSBT) and an eastern subtropical subzone (10IND-5ESBT) distinguished by SSDH = 0.85 m. The northern, equatorial, and Southern Indian Ocean were divided by using the SSDH minimum along the equator and the SSDH maximum along the Tropic of Capricorn.

Southern Ocean

The Southern Ocean overall is a large CO₂ sink where active CO₂ uptake occurs, especially in the subantarctic region during the austral summer, but the high-latitude area releases CO₂ into the atmosphere during ice-free seasons (e.g., Lenton et al. 2013; Landschützer et al. 2015). The TA zones 11SOA, 12SOI, and 13SOP were first distinguished based on a nutrient-depletion line corresponding to SST = 16 °C (11SOA-1SSBT, 12SOI-1SSBT, and 13SOP-1SSBT) in a manner similar to the subtropic-like subzones. The rest of these zones and TA zone 14SSO were further divided into 0.2 m SSDH bands (11SOA-2 to 4, 12SOI-2 to 5, 13SOP-2 to 5, 14SSO-1 to 6) based on the annular variability of the carbonate system in the Southern Ocean (Takahashi et al. 2009). They were divided into austral winter (May–September) and summer (October–April) seasons based on the availability of Chl data. In the Southern Ocean, MLD was not significantly correlated with nDIC residuals (Fig. 17), and we did not use it in the MLR.

References

- Alin SR, Feely RA, Dickson AG, Hernández-Ayón JM, Juraneck LW, Ohman MD, Goericke R (2012) Robust empirical relationships for estimating the carbonate system in the southern California Current System and application to CalCOFI hydrographic cruise data (2005–2011). *J Geophys Res* 117:C05033. <https://doi.org/10.1029/2011JC007511>
- Alory G, Maes C, Delcroix T, Reul N, Illig S (2012) Seasonal dynamics of sea surface salinity off Panama: the far Eastern Pacific Fresh Pool. *J Geophys Res*. <https://doi.org/10.1029/2011JC007802>
- Ayers JM, Lozier MS (2012) Unraveling dynamical controls on the North Pacific carbon sink. *J Geophys Res* 117:C01017. <https://doi.org/10.1029/2011JC007368>
- Bakker DC, Pfeil B, Landa CS et al (2016) A multi-decade record of high-quality *f*CO₂ data in version 3 of the Surface Ocean CO₂ Atlas (SOCAT). *Earth Syst Sci Data* 5:145–153. <https://doi.org/10.5194/essd-5-145-2013>
- Bates NR, Astor YM, Church MJ, Currie K, Dore JE, González-Dávila M, Lorenzoni L, Müller-Karger F, Olafsson J, Santana-Casiano JM (2014) A time-series view of changing ocean chemistry due to ocean uptake of anthropogenic CO₂ and ocean acidification. *Oceanography* 27(1):126–141. <https://doi.org/10.5670/oceanog201416>
- Bates NR, Pequignet AC, Sabine CL (2006) Ocean carbon cycling in the Indian Ocean: 1. Spatiotemporal variability of inorganic carbon and air-sea CO₂ gas exchange. *Global Biogeochem Cycles* 20:GB3020. <https://doi.org/10.1029/2005GB002491>
- de Boyer MC, Madec G, Fischer AS, Lazar A, Iudicone D (2004) Mixed layer depth over the global ocean: an examination of profile data and a profile-based climatology. *J Geophys Res* 109:C12003. <https://doi.org/10.1029/2004JC002378>
- Broullón D, Pérez FF, Velo A, Hoppema M, Olsen A, Takahashi T, Key RM, Tanhua T, González-Dávila M, Jeansson E, Kozyr A, van Heuven SMAC (2019) A global monthly climatology of total alkalinity: a neural network approach. *Earth Syst Sci Data* 11:1109–1127. <https://doi.org/10.5194/essd-11-1109-2019>
- Brown CW, Boutin J, Merlivat L (2015) New insights into *f*CO₂ variability in the tropical eastern Pacific Ocean using SMOS SSS. *Biogeosciences* 12:7315–7329. <https://doi.org/10.5194/bg-12-7315-2015>
- Carter BR, Feely RA, Williams NL, Dickson AG, Fong MB, Takeshita Y (2018) Updated methods for global locally interpolated estimation of alkalinity pH and nitrate. *Limnol Oceanogr Methods* 16(2):119–131. <https://doi.org/10.1002/lom3.10232>
- Chierici M, Fransson A, Nojiri Y (2006) Biogeochemical processes as drivers of surface *f*CO₂ in contrasting provinces in the subarctic North Pacific Ocean. *Global Biogeochem Cycles* 20:GB1009. <https://doi.org/10.1029/2004GB002356>
- Chierici M, Signorini SR, Mattsdotter-Björk M, Fransson A, Olsen A (2012) Surface water *f*CO₂ algorithms for the high-latitude Pacific sector of the Southern Ocean. *Remote Sens Environ* 119:184–196. <https://doi.org/10.1016/j.rse.2011.12.020>
- Chou WC, Tishchenko PY, Chuang KY, Gong GC, Shkirknikova EM, Tishchenko PP (2017) The contrasting behaviors of CO₂ systems in river-dominated and ocean-dominated continental shelves: a case study in the East China Sea and the Peter the Great Bay of the Japan/East Sea in summer 2014. *Mar Chem* 195:50–60. <https://doi.org/10.1016/j.marchem.2017.04.005>
- DeVries T, Holzer M, Primeau F (2017) Recent increase in oceanic carbon uptake driven by weaker upper-ocean overturning. *Nature* 542(7640):215. <https://doi.org/10.1038/nature21068>
- DeVries T, Le Quéré C, Andrews O, Berthet S, Hauck J, Ilyina T, Schwinger J (2019) Decadal trends in the ocean carbon sink. *Proc Natl Acad Sci* 116(24):11646–11651. <https://doi.org/10.1073/pnas.1900371116>
- Denvil-Sommer A, Gehlen M, Vrac M, Mejia C (2019) LSCE-FFNN-v1: a two-step neural network model for the reconstruction of surface ocean *p*CO₂ over the global ocean. *Geosci Model Dev* 12:2091–2105. <https://doi.org/10.5194/gmd-12-2091-2019>
- Fassbender AJ, Sabine CL, Cronin MF, Sutton AJ (2017) Mixed-layer carbon cycling at the Kuroshio extension observatory. *Global Biogeochem Cycles* 31(2):272–288. <https://doi.org/10.1002/2016GB005547>
- Fay AR, McKinley GA (2017) Correlations of surface ocean *p*CO₂ to satellite chlorophyll on monthly to interannual time-scales. *Global Biogeochem Cycles* 31(3):436–455. <https://doi.org/10.1002/2016GB005563>
- Feely RA, Takahashi T, Wanninkhof R, McPhaden MJ, Cosca CE, Sutherland SC, Carr ME (2006) Decadal variability of the air-sea CO₂ fluxes in the equatorial Pacific Ocean. *J Geophys Res*. <https://doi.org/10.1029/2005JC003129>
- Feely R, Wanninkhof R, Takahashi T, Tans P (1999) Influence of El Niño on the equatorial Pacific contribution to atmospheric CO₂ accumulation. *Nature* 398:597–601. <https://doi.org/10.1038/19273>
- Friederich GE, Ledesma J, Ulloa O, Chavez FP (2008) Air–sea carbon dioxide fluxes in the coastal southeastern tropical Pacific *Progress*

- in *Oceanography* 79(2–4):156–166. <https://doi.org/10.1016/j.pcean.2008.10.001>
- Friedlingstein P, Jones MW, O'Sullivan M et al (2019) Global Carbon Budget 2019. *Earth Syst Sci Data* 11:1783–1838. <https://doi.org/10.5194/essd-11-1783-2019>
- Fry CH, Tyrrell T, Achterberg EP (2016) Analysis of longitudinal variations in North Pacific alkalinity to improve predictive algorithms. *Global Biogeochem Cycles* 30:1493–1508. <https://doi.org/10.1002/2016GB005398>
- Garcia HE, Weathers K, Paver CR, Smolyar I, Boyer TP, Locarnini RA, Zweng MM, Mishonov AV, Baranova OK, Seidov D, Reagan JR (2018) World Ocean Atlas 2018 Volume 4: Dissolved Inorganic Nutrients (phosphate, nitrate and nitrate+nitrite, silicate). A. Mishonov Technical Ed.; NOAA Atlas NESDIS 84 pp 35
- Gattuso JP, Magnan A, Billé R et al (2015) Contrasting futures for ocean and society from different anthropogenic CO₂ emissions scenarios. *Science* 349:aac4722. <https://doi.org/10.1126/science.aac4722>
- Gattuso JP, Epitalon JM, Lavigne H, Orr J (2019) seacarb: seawater carbonate chemistry R package version 3.2.12. <https://www.CRANR-project.org/package=seacarb>
- Gruber N, Clement D, Carter BR, Feely RA, van Heuven S, Hoppema M, Ishii M, Key RM, Kozyr A, Lauvset SK, Lo Monaco C, Mathis JT, Murata A, Olsen A, Perez FF, Sabine CL, Tanhua T, Wanninkhof R (2019) The oceanic sink for anthropogenic CO₂ from 1994 to 2007. *Science* 363:1193–1199. <https://doi.org/10.1126/science.aau5153>
- Gruber N, Landschützer P, Lovenduski NS (2019) The variable Southern Ocean carbon sink. *Annu Rev Mar Sci* 11:159–186
- Hashihama F, Kinouchi S, Suwa S, Suzumura M, Kanda J (2013) Sensitive determination of enzymatically labile dissolved organic phosphorus and its vertical profiles in the oligotrophic western North Pacific and East China Sea. *J Oceanogr* 69(3):357–367. <https://doi.org/10.1007/s10872-013-0178-4>
- IOC/UNESCO (2018) Update on IOC Custodianship role in relation to SDG 14 indicators. Fifty-first Session of the Executive Council IOC/EC-LI/2 Annex 6 rev
- IPCC (2013) Climate change 2013: the physical science basis. In: Stocker, TF, D Qin, G-K Plattner, M Tignor, SK Allen, J Boschung, A Nauels, Y Xia, V Bex, PM Midgley (eds.) Contribution of Working Group I to the fifth assessment report of the intergovernmental panel on climate change. Cambridge University Press, Cambridge, United Kingdom and New York, NY, USA, p 1535
- Ibáñez JSP, Diverrès D, Araujo M, Lefèvre N (2015) Seasonal and interannual variability of sea-air CO₂ fluxes in the tropical Atlantic affected by the Amazon River plume. *Global Biogeochem Cycles* 29(10):1640–1655. <https://doi.org/10.1002/2015GB005110>
- Iida Y, Kojima A, Takatani Y, Nakano T, Sugimoto H, Midorikawa T, Ishii M (2015) Trends in pCO₂ and sea–air CO₂ flux over the global open oceans for the last two decades *J Oceanogr*. 71(6) 637–661. [10.1007/s10872-015-0306-4](https://doi.org/10.1007/s10872-015-0306-4)
- Inoue HY, Ishii M, Matsueda H, Aoyama M (1996) Changes in longitudinal distribution of the partial pressure of CO₂ (pCO₂) in the central and western equatorial Pacific, west of 160°W. *Geophys Res Lett* 23:1781–1784. <https://doi.org/10.1029/96GL01674>
- Ishii M, Inoue HY, Midorikawa T, Saito S, Tokieda T, Sasano D, Nakadate A, Nemoto K, Metzl N, Wong CS, Feely RA (2009) Spatial variability and decadal trend of the oceanic CO₂ in the western equatorial Pacific warm/fresh water. *Deep-Sea Res Pt II* 56:591–606. <https://doi.org/10.1016/j.dsr2.2009.01.002>
- Ishii M, Kosugi N, Sasano D, Saito S, Midorikawa T, Inoue HY (2011) Ocean acidification off the south coast of Japan: a result from time series observations of CO₂ parameters from 1994 to 2008. *J Geophys Res Oceans* 116:C06022. <https://doi.org/10.1029/2010JC006831>
- Ishii M, Saito S, Tokieda T, Kawano T, Matsumoto K, Inoue HY (2004) Variability of surface layer CO₂ parameters in the western and central equatorial Pacific. *Global Environmental Changes in the Ocean and on Land*. Eds. Shiyomi M, Kawahata H, Koizumi H, Tsuda A, Awaya Y, TERRAPUB, Tokyo, pp 59–94
- Jones SD, Le Quéré C, Rödenbeck C (2012) Autocorrelation characteristics of surface ocean pCO₂ and air–sea CO₂ fluxes. *Global Biogeochem Cycles*. <https://doi.org/10.1029/2010GB004017>
- Takehi S, Ito SI, Wagawa T (2017) Estimating surface water mixing ratios using salinity and potential alkalinity in the Kuroshio-Oyashio mixed water regions. *J Geophys Res* 122(3):1927–1942. <https://doi.org/10.1002/2016JC012268>
- Key RM, Kozyr A, Sabine CL, Lee K, Wanninkhof R, Bullister JL, Feely RA, Millero FJ, Mordy C, Peng T-H (2004) A global ocean carbon climatology: results from Global Data Analysis Project (GLODAP). *Global Biogeochem Cycles* 18:4031. <https://doi.org/10.1029/2004GB002247>
- Key RM, Tanhua T, Olsen A, Hoppema M, Jutterström S, Schirnick C, van Heuven S, Kozyr A, Lin X, Velo A, Wallace DWR, Mintrop L (2010) The CARINA data synthesis project: introduction and overview. *Earth Syst Sci Data* 2:105–121. <https://doi.org/10.5194/essd-2-105-2010>
- Khaliwala S, Tanhua T, Mikaloff Fletcher S, Gerber M, Doney SC, Graven HD, Gruber N, McKinley GA, Murata A, Ríos AF, Sabine CL (2013) Global ocean storage of anthropogenic carbon. *Biogeosciences* 10:2169–2191. <https://doi.org/10.5194/bg-10-2169-2013>
- Kida S, Mitsudera H, Aoki S et al (2015) Oceanic fronts and jets around Japan: a review. *J Oceanogr* 71:469. <https://doi.org/10.1007/s10872-015-0283-7>
- Kobayashi S, Ota Y, Harada Y et al (2015) The JRA-55 reanalysis: general specifications and basic characteristics. *J Meteor Soc Jpn* 93(1):5–48. <https://doi.org/10.2151/jmsj.2015-001>
- Kosugi N, Sasano D, Ishii M, Enyo K, Saito S (2016) Autumn CO₂ chemistry in the Japan Sea and the impact of discharges from the Changjiang River. *J Geophys Res* 121(8):6536–6549. <https://doi.org/10.1002/2016JC011838>
- Kuragano T, Kamachi M (2000) Global statistical space-time scales of oceanic variability estimated from the TOPEX/POSEIDON altimeter data. *J Geophys Res* 105:955–974. <https://doi.org/10.1029/1999JC900247>
- Körtzinger A (2003) A significant CO₂ sink in the tropical Atlantic Ocean associated with the Amazon River plume. *Geophys Res Lett*. <https://doi.org/10.1029/2003GL018841>
- Körtzinger A, Duinker JC, Mintrop L (1997) Strong CO₂ emissions from the Arabian Sea during south-west monsoon. *Geophys Res Lett* 24(14):1763–1766. <https://doi.org/10.1029/97GL01775>
- Körtzinger A, Send U, Lampitt RS, Hartman S, Wallace DW, Karstensen J, Villagarcia MG, Llinás O, DeGrandpre MD (2008) The seasonal pCO₂ cycle at 49°N/16.5°W in the northeastern Atlantic Ocean and what it tells us about biological productivity. *J Geophys Res*. <https://doi.org/10.1029/2007JC004347>
- Landschützer P, Gruber N, Bakker DCE, Schuster U (2014) Recent variability of the global ocean carbon sink. *Global Biogeochem Cycles* 28:927–949. <https://doi.org/10.1002/2014GB004853>
- Landschützer P, Gruber N, Bakker DCE, Stemmler I, Six KD (2018) Strengthening seasonal marine CO₂ variations due to increasing atmospheric CO₂. *Nat Clim Change* 8:146–150. <https://doi.org/10.1038/s41558-017-0057-x>
- Landschützer P, Gruber N, Haumann FA, Rödenbeck C, Bakker DC, Van Heuven S, Hoppema M, Metzl N, Sweeney C, Takahashi T, Tilbrook B, Wanninkhof R (2015) The reinvigoration of the Southern Ocean carbon sink. *Science* 349(6253):1221–1224. <https://doi.org/10.1126/science.aab2620>
- Landschützer P, Laruelle G, Roobaert A, Regnier P (2020) A combined global ocean pCO₂ climatology combining open ocean and coastal areas (NCEI Accession 0209633). NOAA National

- Centers for Environmental Information. Dataset. 10.25921/qb25-f418. Accessed 2020-06-30
- Lee K, Karl DM, Wanninkhof R, Zhang JZ (2002) Global estimates of net carbon production in the nitrate—depleted tropical and subtropical oceans. *Geophys Res Lett* 29:1907. <https://doi.org/10.1029/2001GL014198>
- Lee K, Tong FJ, Millero FJ, Sabine CL, Dickson AG, Goyet C, Park G-H, Wanninkhof R, Feely RA, Key RM (2006) Global relationships of total alkalinity with salinity and temperature in surface waters of the world's oceans. *Geophys Res Lett* 33:L19605. <https://doi.org/10.1029/2006GL027207>
- Lefèvre N, Diverre D, Gallois F (2010) Origin of CO₂ undersaturation in the western tropical Atlantic. *Tellus* 62B:595–607. <https://doi.org/10.1111/j.1600-0889.2010.00475.x>
- Lefèvre N, Moore G, Aiken J, Watson A, Cooper D, Ling R (1998) Variability of *p*CO₂ in the tropical Atlantic in 1995. *J Geophys Res* 103:5623–5634. <https://doi.org/10.1029/97JC02303>
- Lenton A, Tilbrook B, Law RM et al (2013) Sea-air CO₂ fluxes in the Southern Ocean for the period 1990–2009. *Biogeosciences* 10:4037–4054. <https://doi.org/10.5194/bg-10-4037-2013>
- Leys C, Klein O, Bernard P, Licata L (2013) Detecting outliers: do not use standard deviation around the mean use absolute deviation around the median. *J Exp Soc Psychol* 49(4):764–766. <https://doi.org/10.1016/j.jesp.2013.03.013>
- Maritorena S, d'Andon OHF, Mangin A, Siegel DA (2010) Merged satellite ocean color data products using a bio-optical model: characteristics, benefits and issues. *Remote Sens Environ* 114:1791–1804. <https://doi.org/10.1016/j.rse.2010.04.002>
- Mertens C, Rhein M, Walter M, Böning CW, Behrens E, Kieke D, Steinfeldt R, Stöber U (2014) Circulation and transports in the Newfoundland Basin western subpolar North Atlantic. *J Geophys Res* 119(11):7772–7793. <https://doi.org/10.1002/2014JC010019>
- Midorikawa T, Ishii M, Kosugi N, Sasano D, Nakano T, Saito S, Sakamoto N, Nakano H, Inoue HY (2012) Recent deceleration of oceanic *p*CO₂ increase in the western North Pacific in winter. *Geophys Res Lett* 39:L12601. <https://doi.org/10.1029/2012GL051665>
- Millero FJ, Lee K, Roche M (1998) Distribution of alkalinity in the surface waters of the major oceans. *Mar Chem* 60:111–130. [https://doi.org/10.1016/S0304-4203\(97\)00084-4](https://doi.org/10.1016/S0304-4203(97)00084-4)
- Nakamura T, Maki T, Machida T, Matsueda H, Sawa Y, Niwa Y (2015) Improvement of atmospheric CO₂ inversion analysis at JMA. A31B-0033 (<https://agu.confex.com/agu/fm15/meetingapp.cgi/Paper/64173>) AGU Fall Meeting San Francisco 14–18 Dec. 2015
- Olsen A, Brown KR, Chierici M, Johannessen T, Neill C (2008) Sea surface CO₂ fugacity in the subpolar North Atlantic. *Biogeosciences* 5:535–547. <https://doi.org/10.5194/bg-5-535-2008>
- Olsen A, Key RM, van Heuven S, Lauvset SK, Velo A, Lin X, Schirnick C, Kozyr A, Tanhua T, Hoppema M, Jutterström S, Steinfeldt R, Jeansson E, Ishii M, Pérez FF, Suzuki T (2016) The Global Ocean Data Analysis Project version 2 (GLODAPv2)—an internally consistent data product for the world ocean. *Earth Syst Sci Data* 8:297–323. <https://doi.org/10.5194/essd-8-297-2016>
- Olsen A, Lange N, Key RM et al (2019) GLODAPv2.2019—an update of GLODAPv2. *Earth Syst Sci Data* 11:1437–1461. <https://doi.org/10.5194/essd-11-1437-2019>
- Ono H, Kosugi N, Toyama K, Tsujino H, Kojima A, Enyo K, Iida Y, Nakano T, Ishii M (2019) Acceleration of ocean acidification in the Western North Pacific. *Geophys Res Lett*. <https://doi.org/10.1029/2019GL085121>
- Parard G, Lefèvre N, Boutin J (2010) Sea water fugacity of CO₂ at the PIRATA mooring at 6°S, 10°W. *Tellus* 62B:636–648. <https://doi.org/10.1111/j.1600-0889.2010.00503.x>
- Prytherch J, Brooks IM, Crill PM, Thornton BF, Salisbury DJ, Tjernström M, Anderson LG, Geibel MC, Humborg C (2017) Direct determination of the air-sea CO₂ gas transfer velocity in Arctic sea ice regions. *Geophys Res Lett* 44:3770–3778. <https://doi.org/10.1002/2017GL073593>
- Rio MH, Mulet S, Picot N (2014) Beyond GOCE for the ocean circulation estimate: synergetic use of altimetry, gravimetry, and in situ data provides new insight into geostrophic and Ekman currents. *Geophys Res Lett*. <https://doi.org/10.1002/2014GL061773>
- Ritter R, Landschützer P, Gruber N, Fay AR, Iida Y, Jones S, Nakaoka S, Park G-H, Peylin P, Rödenbeck C, Rodgers KB (2017) Observation-based trends of the Southern Ocean carbon sink. *Geophys Res Lett* 44:12339–12348. <https://doi.org/10.1002/2017GL074837>
- Rodgers KB, Sarmiento JL, Aumont O, Crevoisier C, de Boyer MC, Metzl N (2008) A wintertime uptake window for anthropogenic CO₂ in the North Pacific. *Global Biogeochem Cycles*. <https://doi.org/10.1029/2006GB002920>
- Rosby T (1996) The North Atlantic Current and surrounding waters: at the crossroads. *Rev Geophys* 34(4):463–481. <https://doi.org/10.1029/96RG02214>
- Rödenbeck C, Bakker DC, Gruber N, Iida Y, Jacobson AR, Jones S, Landschützer P, Metzl N, Nakaoka S-I, Olsen A, Park G-H (2015) Data-based estimates of the ocean carbon sink variability—first results of the Surface Ocean *p*CO₂ Mapping intercomparison (SOCOM). *Biogeosciences* 12:7251–7278. <https://doi.org/10.5194/bg-12-7251-2015>
- Sabine CL, Hankin S, Koyuk H et al (2013) Surface Ocean CO₂ Atlas (SOCAT) gridded data products. *Earth Syst Sci Data* 5:145–153. <https://doi.org/10.5194/essd-5-145-2013>
- Sabine CL, Wanninkhof R, Key RM, Goyet C, Millero FJ (2000) Seasonal CO₂ fluxes in the tropical and subtropical Indian Ocean. *Mar Chem* 72:33–53. [https://doi.org/10.1016/S0304-4203\(00\)00064-5](https://doi.org/10.1016/S0304-4203(00)00064-5)
- Sakurai T, Kurihara Y, Kuragano T (2005) Merged satellite and in-situ data global daily SST. In: Proceedings of the 2005 IEEE international geoscience and remote sensing symposium, <https://doi.org/10.1109/IGARSS.2005.1525519>
- Santana-Casiano JM, González-Dávila M, Ucha IR (2009) Carbon dioxide fluxes in the Benguela upwelling system during winter and spring: a comparison between 2005 and 2006. *Deep-Sea Res Pt II* 56:533–541. <https://doi.org/10.1016/j.dsr2.2008.12.010>
- Sarma VVSS (2003) Monthly variability in surface *p*CO₂ and net air-sea CO₂ flux in the Arabian Sea. *J Geophys Res*. <https://doi.org/10.1029/2001JC001062>
- Sarma VVSS, Lenton A, Law R et al (2013) Sea-air CO₂ fluxes in the Indian Ocean between 1990 and 2009. *Biogeosciences* 10:7035–7052. <https://doi.org/10.5194/bgd-10-7035-2013>
- Sarmiento JL, Gruber N (2006) Ocean biogeochemical dynamics. Princeton University Press pp 526
- Schlunegger S, Rodgers KB, Sarmiento JL, Frölicher TL, Dunne JP, Ishii M, Slater R (2019) Emergence of anthropogenic signals in the ocean carbon cycle. *Nat Clim Change* 9:719–725. <https://doi.org/10.1038/s41558-019-0553-2>
- Schuster U, Watson AJ, Bates NR, Corbière A, González-Dávila M, Metzl N, Pierrot D, Santana-Casiano M (2009) Trends in North Atlantic sea-surface *f*CO₂ from 1990 to 2006. *Deep-Sea Res Pt II* 56:620–629. <https://doi.org/10.1016/j.dsr2.2008.12.011>
- Sreeush MG, Rajendran S, Valsala V, Pentakota S, Prasad KVSR, Murtugudde R (2019) Variability trend and controlling factors of Ocean acidification over Western Arabian Sea upwelling region. *Mar Chem* 209:14–24. <https://doi.org/10.1016/j.marchem.2018.12.002>
- Sugimoto H, Hiraishi N, Ishii M, Midorikawa T (2012) A method for estimating the sea-air CO₂ flux in the Pacific Ocean Technical Report of the Meteorological Research Institute 66, pp 32
- Suzuki T, Ishii M, Aoyama M et al. (2013) PACIFICA Data Synthesis Project. ORNL/CDIAC-159, NDP-092. Carbon Dioxide

- Information Analysis Center, Oak Ridge National Laboratory, U.S. Department of Energy, Oak Ridge, Tennessee. https://doi.org/10.3334/CDIAC/OTG.PACIFICA_NDP092
- Takahashi T, Sutherland SC, Chipman DW et al (2014) Climatological distributions of pH, $p\text{CO}_2$, total CO_2 , alkalinity, and CaCO_3 saturation in the global surface ocean, and temporal changes at selected locations. *Mar Chem* 164:95–125. <https://doi.org/10.1016/j.marchem.2014.06.004>
- Takahashi T, Sutherland SC, Sweeney C et al (2002) Global sea–air CO_2 flux based on climatological surface ocean $p\text{CO}_2$, and seasonal biological and temperature effects. *Deep Sea Res Part II* 49(9–10):1601–1622
- Takahashi T, Sutherland SC, Wanninkhof R et al (2009) Climatological mean and decadal change in surface ocean $p\text{CO}_2$ and net sea–air CO_2 flux over the global oceans. *Deep-Sea Res Pt II* 56:554–577. <https://doi.org/10.1016/j.dsr2.2008.12.009>
- Takatani Y, Enyo K, Iida Y, Kojima A, Nakano T, Sasano D, Kosugi N, Midorikawa T, Suzuki T, Ishii M (2014) Relationships between total alkalinity in surface water and sea surface dynamic height in the Pacific Ocean. *J Geophys Res* 119(5):2806–2814. <https://doi.org/10.1002/2013JC009739>
- Toyama K, Rodgers KB, Blanke B, Iudicone D, Ishii M, Aumont O, Sarmiento JL (2017) Large reemergence of anthropogenic carbon into the ocean’s surface mixed layer sustained by the ocean’s overturning circulation. *J Clim* 30:8615–8631. <https://doi.org/10.1175/JCLI-D-16-0725.1>
- Toyoda T, Fujii Y, Yasuda T, Usui N, Iwao T, Kuragano T, Kamachi M (2013) Improved analysis of seasonal–interannual fields using a global ocean data assimilation system. *Theor Appl Mech Jpn* 61:31–48. <https://doi.org/10.11345/nctam6131>
- United Nations (2015) Transforming our world: the 2030 agenda for sustainable development Resolution Adopted by the General Assembly on 25 September 2015 Seventieth Session Agenda Items 15 and 116 A/RES/70/1 https://www.un.org/ga/search/view_doc.asp?symbol=A/RES/70/1&Lang=E
- Wang L, Huang J, Luo Y, Zhao Z (2016) Narrowing the spread in CMIP5 model projections of air–sea CO_2 fluxes. *Sci Rep* 6:37548. <https://doi.org/10.1038/srep37548>
- Wanninkhof R (2014) Relationship between wind speed and gas exchange over the ocean revisited. *Limnol Oceanogr Methods* 12(6):351–362. <https://doi.org/10.4319/lom.2014.12.351>
- Wanninkhof R, Pickers PA, Omar AM et al (2019) A surface ocean CO_2 reference network, SOCONET and associated marine boundary layer CO_2 Measurements. *Front Mar Sci* 6:400. <https://doi.org/10.3389/fmars.2019.00400>
- Watson AJ, Schuster U, Bakker DC, Bates NR, Corbière A, González-Dávila M, Friedrich T, Hauck J, Heinze C, Johannessen T, Körtzinger A (2009) Tracking the variable North Atlantic sink for atmospheric CO_2 . *Science* 326(5958):1391–1393. <https://doi.org/10.1126/science.1177394>
- Weiss R (1974) Carbon dioxide in water and seawater: the solubility of a non-ideal gas. *Mar Chem* 2(3):203–215